Global Estimates of Lunar Surface Elemental Abundances Derived from LRO Diviner Data

Ming Ma[1, 2], Shengbo Chen[2], Tianqi Lu[2], Peng Lu[2], Yu Lu[3, 4], Qin Jin[5]

[1]*School of Surveying and Exploration Engineering, Jilin Jianzhu University, Changchun, China.*
[2]*School of Geo-exploration Science and Techniques, Jilin University, Changchun, China.*
[3] *School of Geographic and Oceanographic Sciences, Nanjing University, Nanjing, China.*
[4]*Jiangsu Center for Collaborative Innovation in Geographical Information Resource Development and Application, Nanjing, China.*
[5]*Space Science Institute, Macau University of Science and Techniques, Macau, China.*

Correspondence to: Shengbo Chen, E-mail：chensb@jlu.edu.cn

Key Points:

• Establishment of global models by univariate regression methods based on the relationships between CF and ground truths

• Development of SiO_2, TiO_2, Al_2O_3, FeO, MgO and CaO abundance maps with resolution of 128 pixels/degree and coverage of 99.86%

• Comparison of the results with Lunar Prospector, Clementine and Chang'E-1 results and application of the results in geological problems

Plain Language Summary

In LRO project, Diviner radiometer now in orbit had been acquired more than 480 billion calibrated radiance values from July 5, 2009 to December 15, 2019. The Standard CF product with the resolution of 128 pixels/degree (237 m/pixel at the equator) and the coverage of 99.86% had been provided by Diviner science team. Considering both resolution and coverage simultaneously, the Standard CF product is the best data source for elemental abundance estimation Therefore, new SiO_2, TiO_2, Al_2O_3, FeO, MgO, CaO maps derived from LRO Diviner data are calculated and presented in this paper. In general, Diviner elemental abundance results are consistent with previous studies such as Clementine and Chang'E-1 results, while Diviner results exhibit better practicability in presenting detailed information for elemental abundances on lunar surfaces and higher accuracy especially on the surface with high latitudes or poor light conditions. Meanwhile, this provides a feasible data source to study the classifications of mare basalt, the inhomogeneity of highland crust and the lunar Mg#.

Abstract

Information on the elemental abundances and distribution is essential for understanding the petrological characteristics and geological evolution of the Moon. In this paper, the thermal infrared data acquired by Lunar Reconnaissance Orbiter (LRO) Diviner are processed to investigate lunar elemental abundances on a global scale (60°N/S) for the first time. The Diviner Level 3 Standard Christiansen feature (CF) product with the resolution of 128 pixels/degree and the coverage of 99.86% is first analyzed and used. The Diviner global models are then established by the univariate regression methods based on the relationships between Diviner CF and ground truths of elemental abundances at 48 lunar sampling sites and the limitations of 1 RMSE of 48 datasets. Finally, the best maps of SiO_2, TiO_2, Al_2O_3, FeO, MgO and CaO abundances considering both resolution and coverage simultaneously are presented and analyzed from global, geologic units, crater and ejecta surfaces. The comparisons indicate that a satisfactory consistency is observed between Diviner results and Clementine or Chang'E (CE)-1 results, while Diviner results exhibit better practicability in presenting detailed information for elemental abundances on lunar surfaces and higher accuracy on the surface with high latitudes or poor light conditions. Meanwhile, it is also demonstrated that Diviner results is the reliable data sources for the applications in classifications of mare basalt, inhomogeneity of highland crust and Mg#.

1. Introduction

In the long evolutionary history, the development and reconstruction of lunar surface layer are dominated by space weathering and impact processes after internal dynamic geological evolution processes such as magmatism, tectonization, seismicity and metamorphism. The surface records the entire history of the interaction with the outside environment. By understanding this history, the evolutionary processes of airless bodies will be better revealed which can be applied to the study of other similar stars within the Solar System. Therefore, as the basic part of lunar surface exploration, the study on elemental abundances and distribution is particularly important. Many remote sensing projects have made this issue their main objective and mission.

Previous groups had estimated elemental abundances based on Earth-based reflectance data (e.g., Charette et al., 1974, 1977); X ray spectroscopy data acquired by Apollo 15 and Apollo 16 (Adler et al., 1972, 1973), SMART-1 (Grande et al., 2004), Chandrayaan-1 (Swinyard et al., 2009; Athiray et al., 2013) or CE-2 (Dong et al., 2016); gamma ray spectroscopy data acquired by Apollo 15 and Apollo 16 (Metzger et al., 1974, 1977), Lunar Prospector (LP) (Lawrence et al., 1998, 1999, 2000, 2002; Prettyman et al., 2006) or SELENE (Kaguya) (Naito et al., 2018); neutron spectroscopy data acquired by LP (Elphic et al., 1998, 2000, 2002; Feldman et al., 1998, 2000); reflectance spectral data acquired by Clementine (Lucey et al., 1995, 1998, 2000, 2006; Sato et al., 2017) or CE-1 (Ling et al., 2011; Yan et al., 2012; Wu, 2012; Sun et al., 2016; Xia et al., 2019). For high energy techniques (such as gamma ray), the relationships between flux of ray energy spectrum and change of elemental energy are the most important theoretical basis. Not only absolute elemental abundances from an average depth of 30 cm (Lawrence et al., 2000; Prettyman et al., 2006), but also some key elemental abundances (such as Th, K, U and O) that can't be detected by any other techniques can be obtained

(Metzger et al., 1977; Lawrence et al., 1999, 2000). For optical reflective techniques with a longer history (Wood, 1912), electronic transition spectral characteristics provide the most direct supports. The relationships between spectral characteristics and elemental abundances had been well studied (Burns, 1970; Hapke et al., 1970; McCord and Adams, 1973; McCord et al., 1981), and the elemental abundance maps had higher resolution and been better developed.

However, there are four obvious problems with the previous results. (1) The usefulness of maps acquired by high energy techniques is limited by lower resolution (Wu, 2012). (2) The coverage of optical maps is poor due to the illumination and topography (Xia et al., 2019), especially in high latitudes or Polar Regions (Lucey et al., 2000; Wu, 2012; Xia et al., 2019). (3) There are no obvious optical diagnostic spectral characteristics in Feldspar, Ilmanite, Glass and Iron except for Pyroxene and Olivine which would increase the uncertainty in the derivation results (Allen et al., 2012). (4) The space weathering (Fischer and Pieters, 1994) and particle sizes (Fischer and Pieters, 1996) also have more significant effects on the reflectance spectrum.

Many groups have payed attention to the thermal infrared techniques (e.g., Paige et al., 2009; Greenhagen et al., 2010; Donaldson et al., 2012; Allen et al., 2012; Tang et al., 2016). In general, the emissivity spectrum of silicate minerals are mainly manifested in complicated condition of Si-O complex ion vibration. It is clear for a prominent emissivity maximum centered near 8 μm called as CF caused by rapid change of the real part of the refractive index before the Christiansen frequency (Conel, 1969). With the increase of silicate mineral polymerization degree, the Si-O bond force constant increases continually which leads the shorter wave shift of the CF wavelength position. For example, the CF of Olivine (15555, LR-CMP-169), Pyroxene Clinopyroxene Augite (70017, LR-CMP-175) and Feldspar Plagioclase (70017, LR-CMP-177) from Reflectance Experiment Laboratory (RELAB) spectrum are 8.578 μm, 8.480 μm and 8.027 μm respectively.

Meanwhile, Si-O_4 tetrahedral complex is connected by metal cations which are definitely connected with the change of Si-O bond force constant, vibration frequency and CF position. The increase of TiO_2, FeO and MgO abundances leads to the longer wavelength of CF, but the increase of Al_2O_3 and CaO abundances leads to the shorter wavelength of CF. In all Apollo samples, the CF of TiO_2-rich (9.48 wt.%), FeO-rich (18.5 wt.%) and MgO-rich (10.8 wt.%) is 8.389 μm (LR-CMP-057, 71061, 20-45 μm), and the CF of Al_2O_3-rich (29.4 wt.%) and CaO-rich (16.1 wt.%) is 8.172 μm (LR-CMP-114, 67461, 20-45 μm). Moreover, comparing to reflectance spectral characteristics, the CF is barely affected by approximate vacuum environment and roughness on lunar surface (Donaldson et al., 2012). Therefore, it can be believed that the CF can be the direct basis for lunar element inversion (Paige et al., 2009).

Until now, Apollo 17 (1972), Clementine (1994), LRO (2009) missions had successively carried infrared scanning radiometer by NASA. In addition to analyzing the thermal physical properties of lunar surface materials, NASA tried to investigate lunar surface oxide abundances using emissivity spectrum (Paige et al., 2009). With thermal infrared data acquired by LRO Diviner in orbit, global CF map (32 pixels/degree) between 60°N/S was calculated and silicate mineralogy abundances were calculated firstly (Greenhagen et al., 2010). Then, the relationships between FeO abundances and CF

were discussed, FeO abundances for three Lunar Pyroclastic Deposits were investigated (Allen et al., 2012) and the highest resolution CF product (128 pixels/degree) was produced (Williams et al., 2017). However, the global maps for SiO_2, TiO_2, Al_2O_3, FeO, MgO and CaO abundances based on Diviner CF did not exist.

This paper presents six global elemental abundance maps (60°N/S) with the highest both resolution and coverage up to now derived from Diviner thermal infrared data. For this purpose, the global models by the univariate regression methods between Diviner CF and ground truths of elemental abundances are established. The six elemental abundance maps are calculated based on Diviner Level 3 Standard CF product with the resolution of 128 pixels/degree and the coverage of 99.86%. Analyses on global, different geologic units, crater and ejecta surfaces are carried out to find the elemental abundances distribution on lunar surface. Comparisons with the results acquired by LP, Clementine and CE-1 are made to investigate the accuracy of Diviner derivation results. Further applications are also tried to verify the usefulness of Diviner elemental abundances in geological problems.

2. Data and methods

2.1 Diviner Level 3 Standard CF products

Diviner is a pushbroom mapping radiometer with nine 21-element arrays detectors onboard LRO launched on June 18, 2009 and still in orbit. The maximum resolution is approximately 200 m (Greenhagen et al., 2010). The fields of view are 320m in track and 160m cross track for 50km altitude (Paige et al., 2009). The detailed instrument description had been given by Paige et al. (2009). In over ten years (July 5, 2009 to December 15, 2019), more than 480 billion calibrated radiance values had been acquired covering a full range of lunar position and time. The data were divided into Experiment Data Record (EDR), Reduced Data Record (RDR), Gridded Data Record (GDR_L2 and GDR_L3) and Polar Resource Products (PRP) by NASA.

Greenhagen et al. (2010) had calculated the effective emissivity and Standard CF using radiance and brightness temperature measurements on the three 8 μm-region channels near 7.55-8.05 μm, 8.10-8.40 μm and 8.38-8.68 μm based on Normalization Emissivity Method (NEM). For each pixel in one RDR data (10 minutes, lunar time), the maximum brightness temperature is firstly calculated using a parabolic fit for three 8 μm-region channels brightness temperature. Meanwhile, the calibrated radiances are binned for each channels. Then the effective emissivity are calculated based on Diviner spectral response and Plank Equation. Finally, another parabolic fit is used to determine the Standard CF which is averaged in one RDR data. The detailed method description had been given by Greenhagen et al. (2010).

For the Diviner GDR Standard CF product calculated by Greenhagen et al. (2010) and the Normalized to Equatorial Noon (MEN) CF product provided by “best effort” of Diviner science team using Diviner data from 2009-07-05 to 2010-11-30, the resolution is 32 pixels/degree and the coverages are 52.4% and 82.5% of lunar surface (60°N/S). As LRO mission proceeds, the Standard CF product with the resolution of 128 pixels/degree had been provided by Diviner science team (Williams et al., 2017) using Diviner data from 2009-07-05 to 2016-10-23. The highest resolution of

CF products is 237 m/pixel at the equator. It means that the resolution of Diviner CF map is slightly lower than 200 m/pixel of CE-1 Interference Imaging Spectrometer (IIM) data, and apparently higher than 1 km of Clementine Ultraviolet-Visible (UV-VIS) data (Lucey et al., 2000) and 15 km of LP Gamma Ray (GR) data (Prettyman et al., 2006).

The 128 pixels/degree Standard CF product has 707,788,800 pixels (46080×15360). There are 1,024,549 pixels (0.14%) with null values that the coverage is 99.86%. The missing pixels are scattered and not concentrated in a specific region. Comparing to 100% of LP GR (Prettyman et al., 2006), 98% of Clementine UV-VIS (Lucey et al., 2000) and 75.4% of CE-1 IIM (Xia et al., 2019), the Diviner CF coverage is the second highest.

For Diviner CF product, the minimum value is 7.00 μm and the maximum value is 9.456 μm. 2,651,599 pixels (0.23%) are between 7.00 μm and 7.80 μm. 610,868 pixels (0.09%) are between 8.55 μm and 9.456 μm. The maximum CF percentage (21.65%) is concentrated in 8.10-8.15 μm (Figure 1). In general, the CF show a Gaussian distribution trend and the average value is 8.1659 μm.

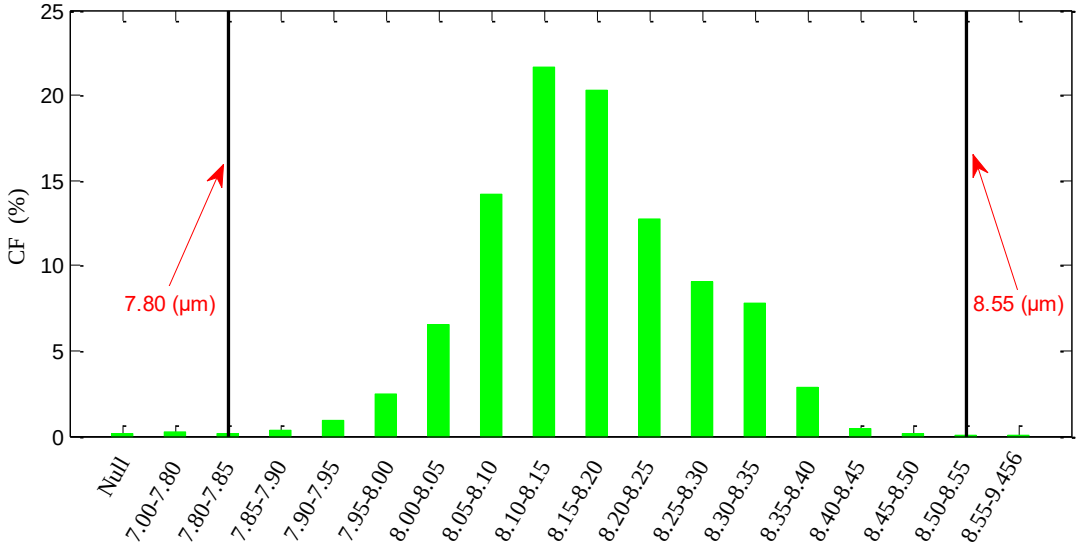

Figure 1. CF Histograms of Diviner Level 3 Standard CF product (128 pixels/degree)

The Diviner Level 3 Standard CF map (60°N/S) is shown in Figure 2. There are approximately uniform CF on the inner of mare surfaces such as Mare Imbrium and Mare Serenitatis, even Mare Orientale and Mare Marginis, whereas CF are constantly changing on highland surface because of small impact events or ejecta from big impact events such as Tycho, Byrgius and Giordano Bruna. On the whole, the difference of global CF between maria and highland is 0.159 μm (8.294-8.135). The maximum difference of mare CF between Mare Tranquillitatis and Mare Orientale (south) is about 0.174 μm (8.352-8.178) The highland CF in the southern hemisphere are significantly higher than those in the northern hemisphere.

The CF on the crater surfaces are the most complex. The older craters such as Plato have higher CF (8.326 μm), whereas younger craters (Copernicus, Kepler, Timocharis, Archimedes et.) are the opposite. The other craters such as Aristarchus and Tsiolkovoskiy show unusual conditions where the CF of the central peak and wall are 0.2 μm lower than those of the plain. On the surfaces of the South

Pole-Aitken (SPA) basin, the CF are the intermediate value between maria and highland. Meanwhile, compared to reflectance maps there are more intuitive differences. The CF on plain and mare surfaces are higher than that on wall and highland surface where reflectance values are the opposite. In other word, bright and dark in reflectance map are interchanged in CF map.

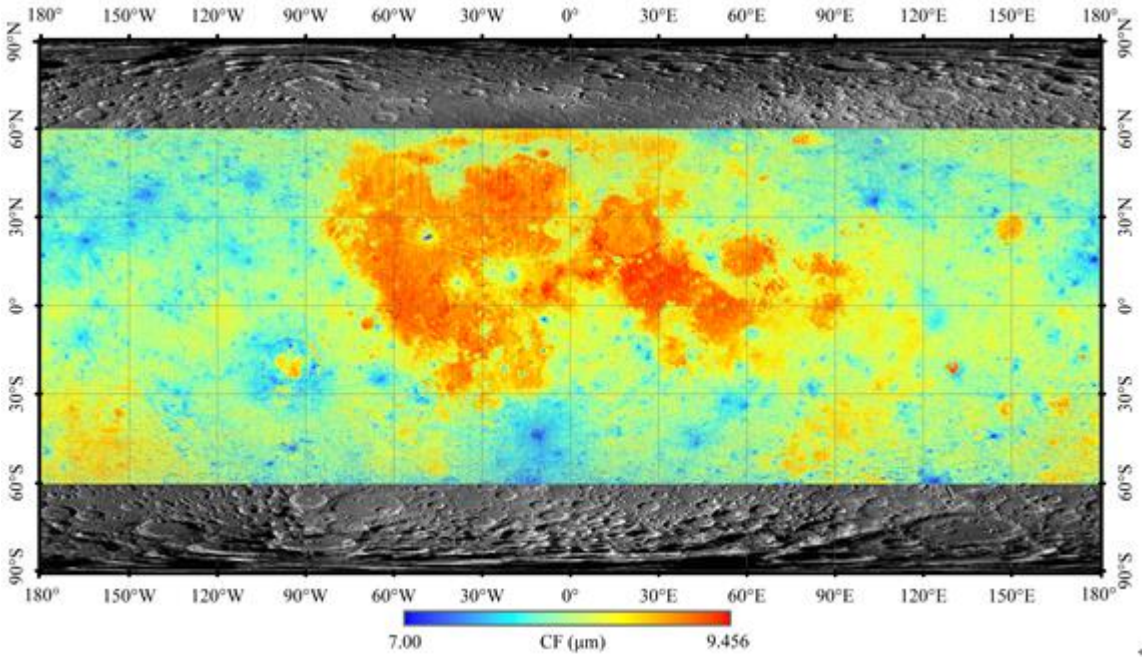

Figure 2. The Diviner Level 3 Standard CF map (60°N/S). The projection system is GCS_moon_2000. The resolution is 128 pixels/degree (237 m/pixel at the equator). The coverage is over 99.86% (1,024,549 null in 707,788,800 pixels). The map scale is 1:250,000,000. The upper and lower limits of CF are shown in the legend. The base map is LRO Wide Angle Camera (WAC) map of 100 meters/pixel (Scholten et al., 2012).

2.2 Elemental abundances and Diviner CF for lunar sites

Until now, based on elemental abundance measurements from the returned samples or actual location with geographic information (Lucey et al., 2000; Liu et al., 2015), 48 lunar sampling sites can be confirmed including 44 Apollo sites (11, 12, 14, 15, 16, 17), 3 Luna sites (16, 20, 24) (Blewett et al., 1997, Jolliff et al., 1999; Lucey et al., 2000) and CE-3 site (Wu et al., 2018). With the elemental abundances of 118+6 Apollo samples, 3 Luna samples (Blewett et al., 1997, Jolliff et al., 1999; Lucey et al., 2000) and CE-3 rover measurements (Wu et al., 2018), the mean abundances of six elements in 48 lunar sites are recalculated (Table 2). The mean abundance values of Apollo samples can eliminate the unreliable abundances of a particular element in the particular sample and be a better indicator for the site compositions.

For six elements, the mean SiO_2 abundance is 44.2853 wt.% and the standard deviation (STD) is 2.1417 wt.% which demonstrates the nearly uniform distribution of lunar surface silicate minerals. However, there are obvious differences in the abundances of other five elements, especially Al_2O_3 (STD of 5.6438 wt.%) and FeO (STD of 4.8219 wt.%). The TiO_2, FeO and MgO abundances on Apollo 16 site in the highland are significantly lower than in other Apollo sites in the maria, while the Al_2O_3 and CaO abundances are the opposite. The elements abundances of Apollo 14 confirm that the site is located a transitional region between highland and maria. The biggest differences of SiO2,

211 TiO_2, Al_2O_3, FeO, MgO, CaO are 8.40 wt.%, 9.60 wt.%, 19.07 wt.%, 18.29 wt.%, 7.15 wt.%, 8.37
212 wt.% respectively. Moreover, the relationship between SiO_2, Al_2O_3, CaO and TiO_2, FeO, MgO show
213 inversely correlation (Heiken et al., 1991) which provides a verification indication for the elemental
214 abundances of mare and highland surface.

215 Table 2 The elemental abundances (wt.%) and CF (μm) for 48 lunar sampling sites used in this study.

Lunar Sites	SiO_2	TiO_2	Al_2O_3	FeO	MgO	CaO	CF
A11	41.4	7.5	13.455	15.8	7.91	12.275	8.377
A12	46.216	3.08	13.77	15.48	9.79	10.54	8.298
A14-LM	48.2	1.73	17.69	10.5	9.52	10.32	8.265
A14-Cone	47.536	1.6	17.533	10.3	9.565	10.95	8.198
A15-LM	46.75	1.9	14.265	15	10.585	10.27	8.266
A15-S1	46.8	1.6	13.2	16.8	10.7	10.25	8.290
A15-S2	46.315	1.3	17.378	11.5	10.54	11.53	8.320
A15-S4	46.26	1.2	13.4	16.6	11.6	8.9	8.235
A15-S6	46.768	1.5	16.45	12.1	10.475	10.975	8.256
A15-S7	46.29	1.1	15.3	13.9	11.567	10.267	8.291
A15-S8	46.75	1.7	14.45	15.2	10.65	10.25	8.285
A15-S9	46.46	1.8	12.5	16.9	11	9.8	8.320
A15-S9a	46.52	2	10.3	20.4	11.25	8.3	8.281
A16-LM	45.285	0.6	26.575	5.6	6.15	15.78	8.155
A16-S1	44.846	0.6	26.714	5.4	6.056	15.604	8.165
A16-S2	44.575	0.593	26.73	5.44	6.477	15.55	8.163
A16-S4	45.067	0.537	27.53	4.853	5.36	15.71	8.137
A16-S5	45.063	0.7	26.187	5.9	6.183	15.063	8.184
A16-S6	45.135	0.7	27.133	6	6.867	16.4	8.180
A16-S8	45.078	0.6	26.545	5.4	6.223	15.365	8.175
A16-S9	44.88	0.6	26.283	5.7	6.343	15.49	8.178
A16-S11	45.142	0.372	29.372	3.95	4.455	16.67	8.048
A16-S13	45.015	0.5	28.067	4.8	6	14.65	8.078
A17-LM	40.8	8.5	12.1	16.6	9.8	11.1	8.262
A17-S1	39.9	9.6	10.9	17.8	9.6	10.8	8.338
A17-S2	45	1.5	20.7	8.7	9.9	12.8	8.213
A17-S3	44.9	1.8	20.4	8.7	10.2	12.9	8.263
A17-S5	39.8	9.9	10.9	17.7	9.6	10.8	8.303
A17-S6	43.5	3.4	18.3	10.7	10.8	12.2	8.234
A17-S7	43.7	3.9	17.	11.6	10.1	11.9	8.231
A17-S8	43.4	4.04	16.68	12.24	10.42	11.56	8.307
A17-S9	42.1	6.4	13.9	15.4	10	11.3	8.317
A17-LRV1	41.3	8	12.6	16.3	9.4	11.2	8.333
A17-LRV2	43.1	4.4	16.1	13.4	10.3	11.9	8.307
A17-LRV3	42.2	5.5	14.4	14.8	10.4	11.3	8.302
A17-LRV4/S2a	44.9	1.3	21.4	8.5	9.6	12.8	8.141
A17-LRV5	44.8	1.3	21.4	8.5	9.6	12.8	8.282
A17-LRV6	44.5	2.6	19.4	10.3	9.9	12.5	8.258

A17-LRV7	41.8	6.8	12.8	16.1	10.3	10.7	8.311
A17-LRV8	41.9	6.6	13.5	15.7	9.9	11.3	8.345
A17-LRV9	42.2	6.1	14.3	14.6	9.8	11.3	8.321
A17-LRV10	43.5	3.7	17.5	11.2	10.5	12.1	8.272
A17-LRV11	43.2	4.5	16.3	12.7	10	11.9	8.312
A17-LRV12	39.9	9.97	11.2	17.4	9.36	10.8	8.324
Luna 16	41.7	3.3	15.3	16.7	8.8	12.5	8.341
Luna 20	45.6	0.5	22.9	7.5	9.15	14.5	8.239
Luna 24	45.36	1.0	12.1	19.6	10	11.1	8.359
CE-3	-	4.31	12.11	22.24	8.61	9.72	8.362

Description: References for compositions see Lucey et al. (2000, Table 1), Jolliff et al. (1999, Table 4) and Blewett et al. (1997, Table1). The increased samples are 12029 (A12), 62231(A16-S2, Size of 20-45 μm), 64801 (A16-S4), 67711 (A16-S11) and 78481 (A17-S8). The composition of A15-LM comes from 15013 and 15021, A16-S6 comes from 66031, 66041 and 66081, CE-3 comes from Wu et al. (2018). References for Latitude and Longitude of Apollo and Luna sites see Lucey et al. (2000, Table1) and CE-3 site see Liu et al. (2015). The CF are manually extracted from Diviner Level 3 Standard CF products.

For Apollo, Luna and CE-3 missions, the detecting areas of lunar surface had expanded from a few hundred square meters at Apollo 11 to tens of thousands of square meters at Apollo 17. Correspondingly, with the maximum resolution of 237 m, the CF are manually extracted from Diviner Level 3 Standard CF map depending on the sample returned sites (Lucey et al., 2000) or the rover measured position (Liu et al., 2015) of 1×1 pixels (Table 2). In remote sensing data, the CF of lunar sites have obvious regularity and rationality. The CF of Apollo 11, 12, 15, 17, Luna 16, 20, 24 and CE-3 in maria are obviously higher than that of Apollo 16 in highland, and the maximum difference is 0.329 μm (A11 and A16-S11). It's inferred again that Apollo 14 is not really highland because the CF extracted from the map are between highland and mare values.

2.3 Mathematical modelling

For six elements, the relationships between Diviner CF and FeO abundance had been discussed using linear regression (Allen et al., 2012). But, SiO_2, TiO_2, Al_2O_3, MgO and CaO abundances have not been correlated with CF. Therefore, six univariate regression models (exponential, exponential, linear, quadratic, cubic, logarithmic) are used for experimental analysis and the best models are determined with the highest R-square (R^2).

The returned samples and field measurement have certain representativeness and randomness. Diviner thermal infrared data are also comprehensive information within tens of thousands of square meters. These two factors together lead to predictable error in the determination of elemental abundances or Diviner CF at the sampling pixels. In the initial relationships of 48 datasets, the same conclusion can be obtained. The R^2 of SiO_2, TiO_2, Al_2O_3, FeO, MgO and CaO models are 0.1546, 0.3894, 0.7491, 0.7136, 0.4655 and 0.5376 respectively. Hence, before establishing the Diviner prediction models, the outliers of 48 datasets are analyzed and culled firstly. Because the outliers can reduce the accuracy of models and prediction results that the influence should be eliminated.

In this study, the outlier rejections are tested repeatedly by 2, 1.5, 1 and 0.5 Root Mean Square

Error (RMSE) of 48 datasets. For example FeO (Figure 3), the RMSE of 48 dataset is 2.608. Under the limitations of 2, 1.5, 1 and 0.5 RMSE, the number of samples decreases from 48 to 16 and the R^2 of models increases from 0.7136 to 0.9622 which illustrates the need for constraints. However, excessive rejection make no sense. 1 RMSE (Figure 3, Green line) is selected based on error theory and experimental data. Finally, the relationships between Diviner CF and elemental abundances for sampling pixels are established and thermal infrared prediction models are provided.

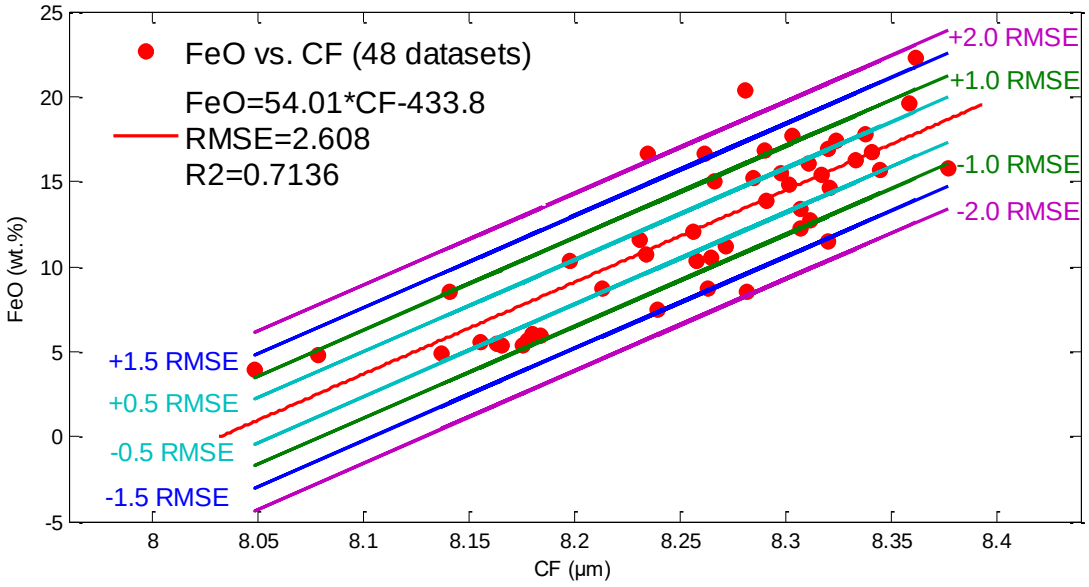

Figure 3. The relationship between FeO abundance and Diviner CF for 48 lunar sampling sites and the outlier rejections of 48 datasets.

3. Results

3.1 Diviner models

Six univariate regression types of approaches were chosen to build the relationships between Diviner CF and elemental abundances at 48 lunar sampling sites. The relationships with the highest R^2 were selected. Except for TiO_2 that the relationship can be described as an exponential correlation, the relationships of the other five oxides can be described as linear correlations.

The points under the limitations of 1 RMSE of 48 datasets were regressed using both linear and exponential relationships. Figure 4 shows the relationship with the highest R^2 value, for each of the six oxides tested in this study. The linear R^2 of Al_2O_3 is highest (0.9043), followed FeO (0.8843), MgO (0.7853), CaO (0.7504) and R^2 of SiO_2 is lowest (0.604). The exponential R^2 of TiO_2 is 0.704 and only higher than the linear R^2 of SiO_2. Thus, it can be speculated that the prediction accuracy of Al_2O_3 and FeO is higher than that of MgO, CaO and TiO_2, the deviation of SiO_2 is largest.

For six Diviner models, the models are described by the regression slope (p1, p2 or a, b). The SiO_2, Al_2O_3, CaO abundances are positively correlated with CF, whereas the TiO_2, MgO, FeO abundances are negatively correlated with CF. It means that the influences of SiO_2, Al_2O_3, CaO abundances on CF are weaker near longer wavelength position (8.55) and stronger near the shorter wavelength position (7.80), whereas that of TiO_2, MgO, FeO abundances are the opposite. Thus, the CF of 7.00 to 7.80 μm or 8.55 to 9.456 μm should be deleted during calculating surface elemental

abundances. Moreover, the maximum elemental abundances from 806 published Apollo samples should be added to the prediction results, especially for the exponential correlation of TiO2 (14.5 wt.%, 77538).

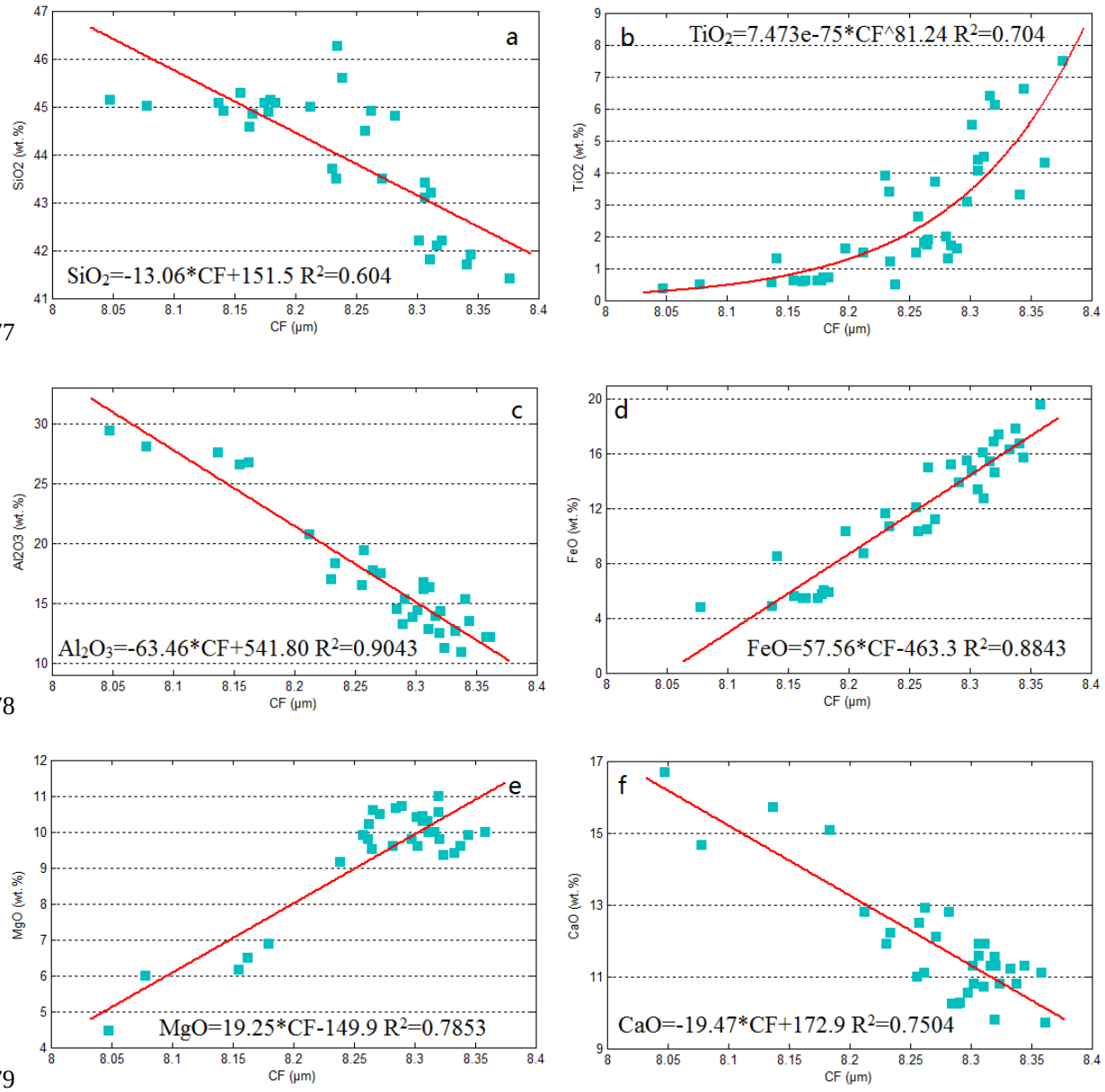

Figure 4. The relationships between Diviner CF and elemental abundances under the limitations of 1 RMSE of 48 datasets. The number of points SiO_2, TiO_2, Al_2O_3, FeO, MgO and CaO are 30, 38, 31, 35, 31and 33 respectively.

3.2 Prediction Results

3.2.1 Global

707.7 million elemental abundance values are calculated from the Diviner Level 3 Standard CF map (60°N/S) based on Diviner models. Six separate maps are produced with the resolution of 128 pixels/degree and the coverage of over 99% (Figure 5). After deleting the null pixels, global average elemental abundances of SiO_2, TiO_2, Al_2O_3, FeO, MgO and CaO are 44.85 wt.%, 1.46 wt.%, 23.60 wt.%, 7.82 wt.%, 7.29 wt.% and 13.91 wt.% respectively and the total is 98.93 wt.%.

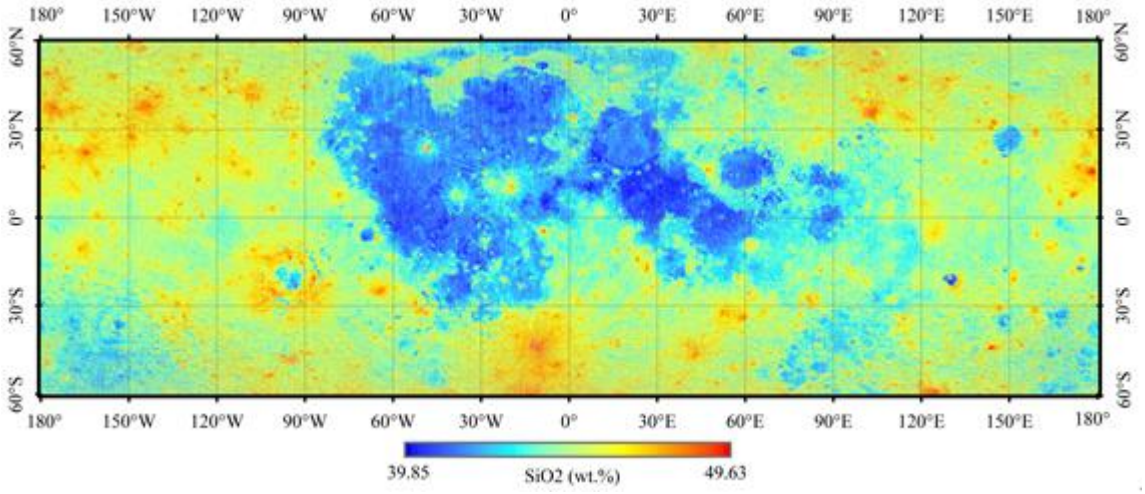
180° 150°W 120°W 90°W 60°W 30°W 0° 30°E 60°E 90°E 120°E 150°E 180°
60°N 30°N 0° 30°S 60°S
39.85
SiO2 (wt.%)
49.63

(a)

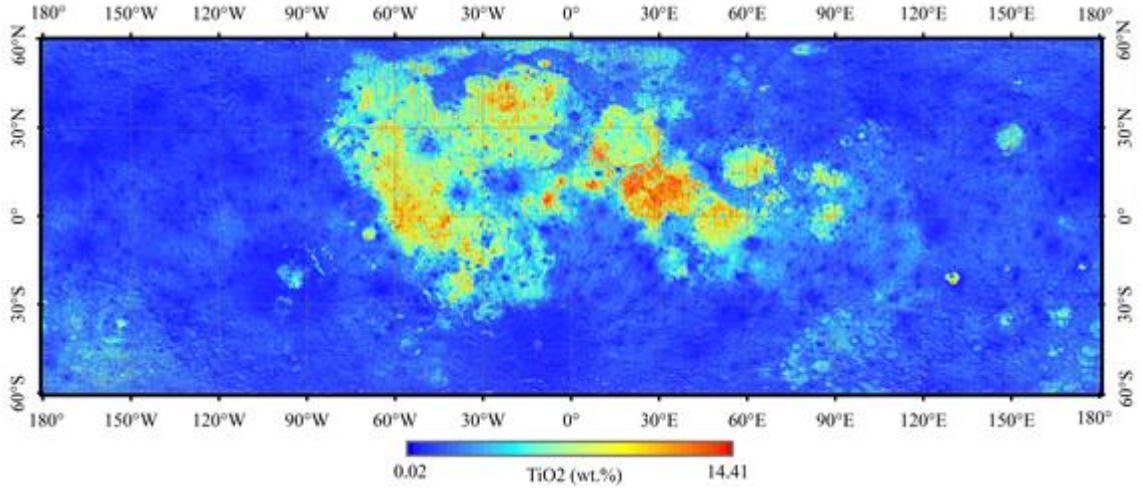
180° 150°W 120°W 90°W 60°W 30°W 0° 30°E 60°E 90°E 120°E 150°E 180°
60°N 30°N 0° 30°S 60°S
0.02
TiO2 (wt.%)
14.41

(b)

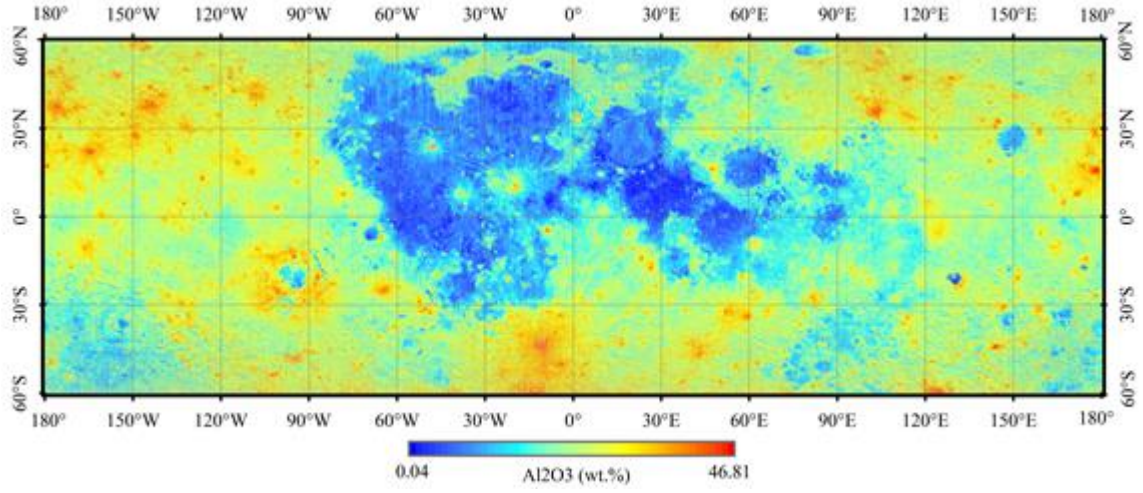
180° 150°W 120°W 90°W 60°W 30°W 0° 30°E 60°E 90°E 120°E 150°E 180°
60°N 30°N 0° 30°S 60°S
0.04
Al2O3 (wt.%)
46.81

(c)

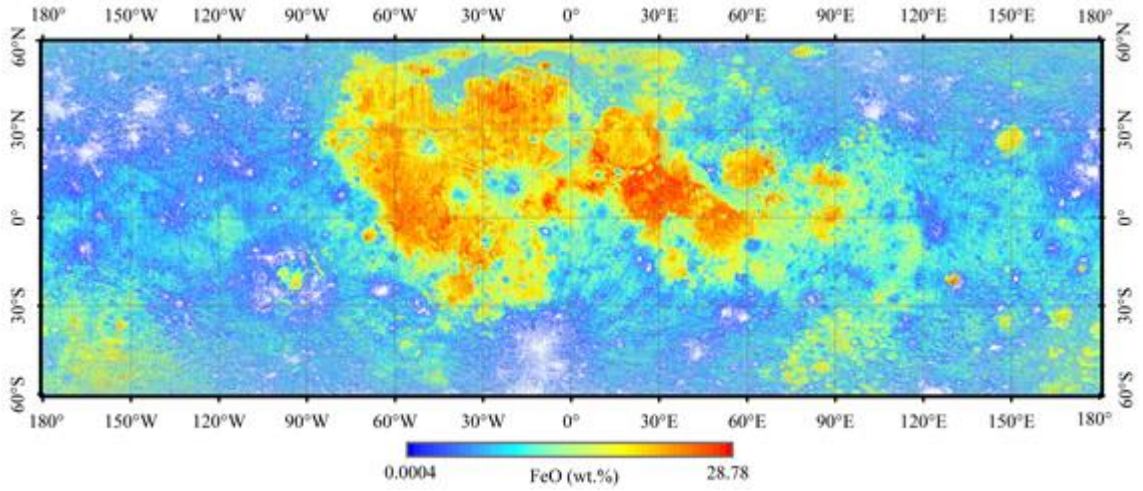

(d)

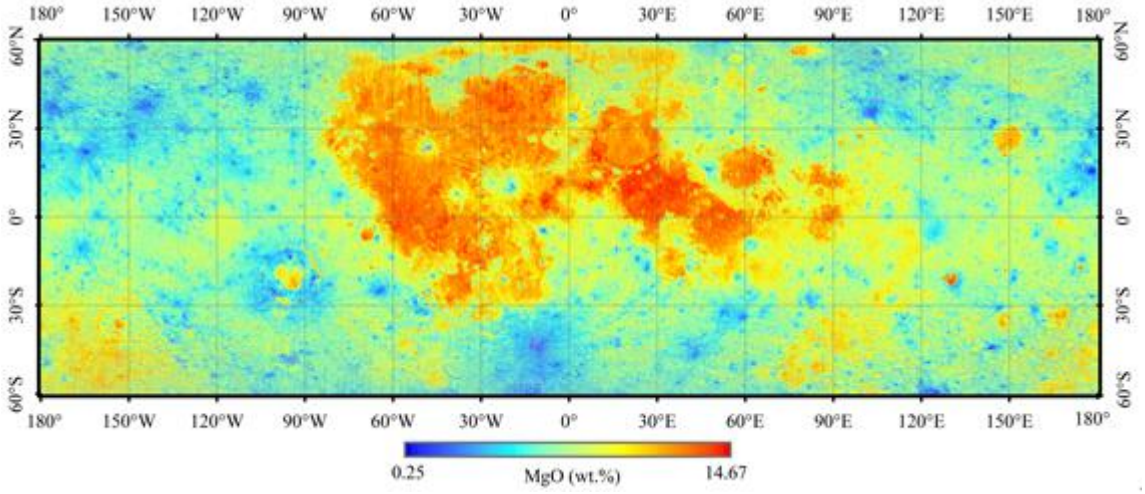

(e)

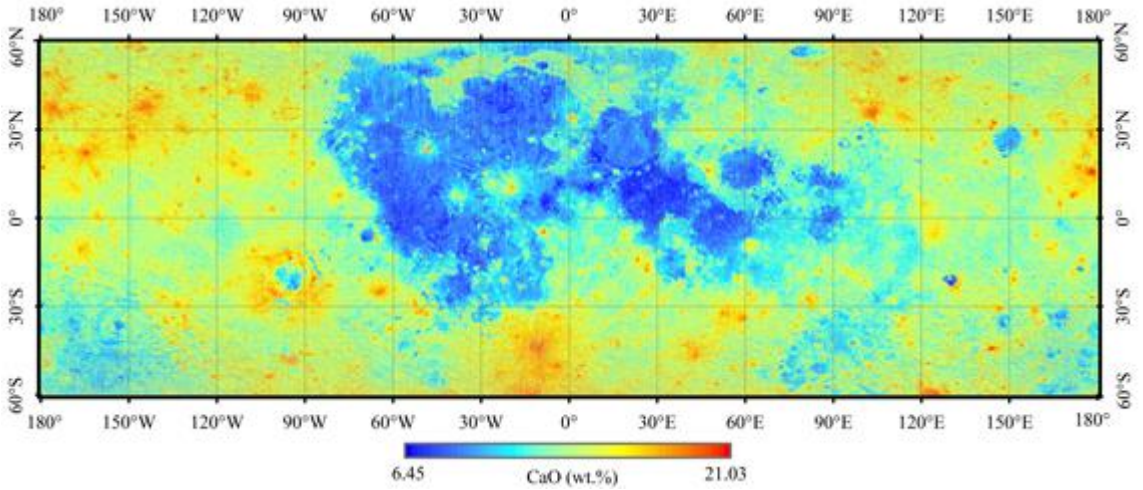

(f)

Figure 5. The maps of six elemental abundances calculated from the Diviner Level 3 Standard CF map. (a) SiO_2 abundance map, (b) TiO_2 abundance map, (c) Al_2O_3 abundance map, (d) FeO abundance map, (e) MgO abundance map, (f) CaO abundance map. The white pixel is 0 value in FeO abundance map (d). Referring to Figure 2 for geographic information. The upper and lower limits of each elemental abundance are shown in the legend.

Corresponding to positive and negative correlations, TiO_2, FeO and MgO abundances increase

obviously with the increase of CF on typical mare surfaces while SiO_2, Al_2O_3 and CaO abundances decrease. It is the opposite on highland surface. But on separate geological unit surfaces such as SPA basin there are an approximately uniform distribution of six elemental abundances.

On global surfaces (Figure 6) some of abundance differences can be made by craters and ejecta where big and systematic differences in average elemental abundances are presented (Table 2). On the mare surfaces, FeO (14.14 wt.%) and Al_2O_3 (15.49 wt.%) are higher than CaO (11.42 wt.%), MgO (9.76 wt.%) and TiO_2 (3.76 wt.%), while on the highland surface, Al_2O_3 (25.51 wt.%) and CaO (14.50 wt.%) are higher than FeO (6.14 wt.%), MgO (6.71 wt.%) and TiO_2 (0.94 wt.%). Especially on SPA basin surface, six elemental abundances are the intermediate values between maria and highland and is close to the global average elemental abundances.

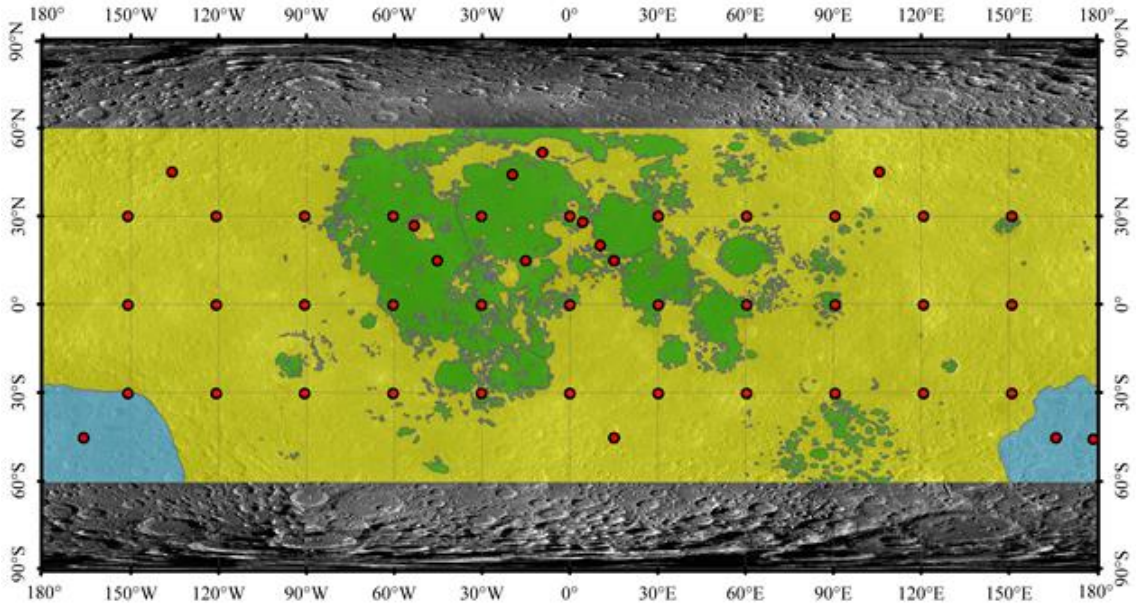

Figure 6. The areas (60°N/S) of three large geological units including maria, highland and SPA basin. The green area are maria and crater plains (Nelson et al., 2010), the yellow area is highland (Nelson et al., 2010), and the wathet blue area is SPA basin by this study, the red points are 47 verification points with the size of 0.078125°×0.078125°. Referring to Figure 2 for geographic information and the base map.

Table 2 The average values and proportions of elemental abundances on maria, highland and SPA surface

	Average (wt.%)				Proportions (%)		
	Global	Maria	Highland	SPA	Maria	Highland	Basin
SiO_2	44.85	43.19	45.25	44.57	16.65	78.04	5.31
TiO_2	1.46	3.76	0.94	1.57	44.52	49.75	5.73
Al_2O_3	23.60	15.49	25.51	22.24	11.35	83.62	5.04
FeO	7.82	14.14	6.14	8.71	34.71	59.06	6.23
MgO	7.29	9.75	6.71	7.71	23.13	71.22	5.65
CaO	13.91	11.42	14.50	13.49	14.20	80.61	5.18

It's obvious that the proportions of six elemental abundances in each geological unit are different (table 2). For TiO_2, mare surfaces have almost the same abundances with highland surface. For FeO and MgO, mare surfaces have 34.71% and 23.13% of the global abundances corresponding to 59.06% and 71.22% in highland. Increasing differences, percentage of SiO_2 is 16.65% in maria

and 78.04% in highland. Maximally for CaO and Al_2O_3, the difference between maria and highland is 66.41% and 72.27%. The SPA Basin surface have almost a similar percentage of six elemental abundances which are 5.18% to 6.23%.

3.2.2 Maria, Highland and SPA

The mean elemental abundances of major maria are showed in table 3. On mare plain surfaces of nearside such as Mare Tranquillitatis, TiO_2, FeO, MgO abundances are highest and SiO_2,Al_2O_3, CaO abundances are lowest on all mare surfaces. On Oceanus Procellarum and Mare Inbrium surfaces with the vast area, the Aristarchus and Timocharis impact events don't substantially change elemental abundances, but slightly increased SiO_2, Al_2O_3, CaO abundances and decreased TiO_2, FeO, MgO abundances. It is more obvious for these differences between Oceanus Procellarum (south) and Oceanus Procellarum surfaces. The mare surfaces surrounded by highland or in high latitudes such as Mare Humboldtianum or Mare Frigoris, TiO_2, FeO, MgO abundances are lower and SiO_2, Al_2O_3, CaO abundances are higher where elemental abundances are seriously disturbed by the highland anorthosite materials and the boundary is getting blurry. On the farside, two maria including Mare Orientale and Mare Moscoviense (Mare Ingenii located in SPA basin) are surrounded by highland and have incomprehensible material distribution especially at the boundary because of the unique geological structure and the random distribution of highland anorthosite materials. It is also obvious for Mre Orientale (south) surfaces that TiO_2, FeO, MgO abundances are lowest and SiO_2,Al_2O_3, CaO abundances are highest. In a word, on the farside each mare element abundance is similar to that on highland surface and the mare material characteristics become indistinct.

Table 4 The mean values of six elemental abundances of lunar major maria (wt.%)

Mare	SiO_2	TiO_2	Al_2O_3	FeO	MgO	CaO
Anguis	43.89	2.26	18.92	11.07	8.71	12.48
Australe	44.06	1.98	19.72	10.41	8.47	12.72
Cognitum	43.18	3.50	15.48	14.12	9.75	11.42
Crisium	43.06	3.99	14.89	14.65	9.93	11.24
Fecunditatis	42.98	4.20	14.51	14.98	10.05	11.12
Frigoris	43.76	2.50	18.29	11.71	8.90	12.28
Humboldtianum	44.33	1.82	21.09	9.39	8.05	13.14
Humorum	43.21	3.59	15.59	14.05	9.72	11.45
Imbrium	42.97	4.19	14.46	15.03	10.06	11.11
Insularum	43.47	2.94	16.88	12.88	9.33	11.85
Marginis	43.17	3.62	15.40	14.17	9.78	11.40
Moscoviense	43.33	3.11	16.17	13.47	9.54	11.63
Nectaris	43.53	2.75	17.17	12.58	9.24	11.94
Nubium	43.65	2.52	17.76	12.08	9.06	12.12
Orientale	44.13	1.87	20.08	10.03	8.36	12.83
Orientale (south)	**44.69**	**1.23**	**22.79**	**7.74**	**7.54**	**13.66**
Serenitatis	42.83	4.49	13.77	15.65	10.27	10.90
Smythii	43.00	4.02	14.59	14.92	10.03	11.15
Spumans	43.09	3.68	15.03	14.50	9.89	11.28

Temporis	44.41	1.40	21.46	8.71	7.94	13.26
Tranquillitatis	**42.42**	**6.19**	**11.77**	**17.46**	**10.88**	**10.28**
Undarum	42.93	4.21	14.25	15.21	10.13	11.04
Vaporum	42.87	4.39	13.95	15.48	10.22	10.95
Oceanus Procellarum	42.99	4.13	14.56	14.96	10.03	11.14
Oceanus Procellarum (south)	43.42	2.90	16.63	13.07	9.41	11.77

Description: The bold value is the extreme value located in Mare Orientale (south) and Mare Tranquillitatis respectively

Highland surface are characterized by higher SiO_2, Al_2O_3, CaO and lower TiO_2, FeO, MgO. However, each abundance is not uniformly distributed. The high SiO_2, Al_2O_3 and CaO abundances are mainly concentrated on Tycho, Byrgrius, Wegener, Sterinus and Giordano Bruno crater and ejecta surfaces and the periphery of Mare Orientale. The FeO and MgO abundances are evenly distributed on highland surface where these are higher on the southern and eastern hemisphere in contrast to the northern and western hemisphere except for crater and ejecta surfaces. Remarkably, TiO_2 abundance is almost zero on whole highland surface.

The SPA basin is a special geological unit and elemental abundances are different from maria and highland. TiO_2, FeO and MgO abundances are lower than that on mare surfaces and Al_2O_3, CaO abundances are too lower than that on highland surface. The abundance differences of SPA plain surface between any two elements are the most indistinct in all geological units.

3.2.3 Crater and ejecta

On the largest number of craters and ejecta surfaces, elemental distribution is characteristic and discussed separately. In maria, Kepler and Copernicus crater and ejecta surfaces typically have higher SiO_2, Al_2O_3, CaO abundances and lower TiO_2, FeO, MgO abundances than the surrounding surfaces. The similar situations may occur on Aristarchus, Seleucus, Kraff, Cardanus, Timocharis, Timochari crater and ejecta surfaces. However, On the surfaces of Herodotus to east of Aristarchus, Prinz to northwest of Aristarchus, Eratosthenes, lambert, C.herschel around Copernicus, Archimedes, Autolycus around Aristillus, each element abundance is roughly the same as that on the surrounding areas where the abundance boundary of impact crater appears to disappear.

In highland, most craters and all ejecta surfaces have higher SiO_2, Al_2O_3, CaO abundances and lower TiO_2, FeO, MgO abundances. Another areas of such abundance are the highland around Mare Orientale where the area is almost the same as that of Tycho crater and ejecta. However, a few craters including Plato and Lomonosov are exceptions where crater plains surfaces are filled with more TiO_2, FeO, MgO and the crater rim have more SiO_2, Al_2O_3, CaO. The central peak of several craters including Tsiolkovskiy and Aitken but not Tycho have obvious elemental abundance difference compared with the impact crater plains.

4. Discussions

4.1 Model analysis

As repeatedly mentioned above, this study's models are the "global" thermal infrared models in which all of the sampling point information have been used. However, the correlations of the initial relationships of 48 datasets are relatively lower. There are some reasons among which two factors

must be mainly mentioned.

One is the representativeness of elemental abundances of lunar samples or rover measurements. Traditionally, elemental abundances of each sampling pixel had been determined by the average abundance value of 1-12 samples. The problems whether the values can accurately characterize the elemental abundance of sampling pixel and what is the right number of sampling pixels are one topic worthy of discussion. For the establishment of Diviner models, more sampling points and wider sample selection can provide reliable data sources. For example, the number of samples and sampling pixels of Lucey et al. (2000) for modeling are 118 and 47; Wu (2012) are 76 and 18; Xia et al. (2019) are 100 and 39; this study are 124 and 48. Each group hopes to improve the usefulness and accuracy of the models by increasing the representativeness of the ground truth value. However, it may be one of the universal problems in the process of remote sensing modeling, because the number of sampling sites is limited and most are concentrated in mare of nearside except for Apollo 17.

The other is the accuracy of the spectral values of mixed pixel. Even in the smallest remote sensing pixel, mixed substances are also present. Adding to the effects of topography and scale, remote sensing data are all mixed information. The problem whether the measurements can accurately characterize the spectral values of mixed pixel is another topic worthy of discussion. With the different resolutions, the number of pixels for modeling represented by the measurement of Clementine, LP, CE-1 and Diviner is different. For example, the number of Lucey et al. (2000) is from 1×1 to 6×6 pixels; Wu (2012) is from 2×2 to 10×10 pixels; Xia et al. (2019) is 1×1 pixel; this study is 1×1 pixel. Theoretically, in the smaller spatial scale, the remote sensing measurement can better represent the spectral characteristics of mixed pixel. Therefore, the 1×1 pixel is more reasonable for modeling. Meanwhile, mixed spectral decomposition (Villa et al., 2010) has been studied for a long time, but a few potential complexities have not been fully explored and the result is always unsatisfactory.

The above two reasons jointly determine the relationships between elemental abundances and CF in Diviner models. In addition to selecting all current sampling pixels with ground truth value, trial and error of the two methods are also performed in our study.

One is to increase the number of CF pixels in order to obtain high R^2. For example FeO (Figure 7), with the pixels increasing from 1×1 to 21×21, the R^2 first increase and then decrease, the maximum R^2 is 0.7776 with 9×9 pixels (2×2km) that the same area was used by Allen et al. (2012). The similar thing happens with the other five oxides except that the maximum R^2 is different for 0.1652 of SiO_2 (5×5 pixels), 0.4358 of TiO_2 (3×3 pixels), 0.8381 of Al_2O_3 (9×9 pixels), 0.6045 of MgO (13×13 pixels) and 0.6632 of CaO (15×15 pixels) respectively. These demonstrates the uncertainty of elemental abundances and Diviner CF in pixels. No obvious regularity is found. The R^2 don't improve significantly too, especially for SiO_2. Therefore, the outliers can only be eliminated.

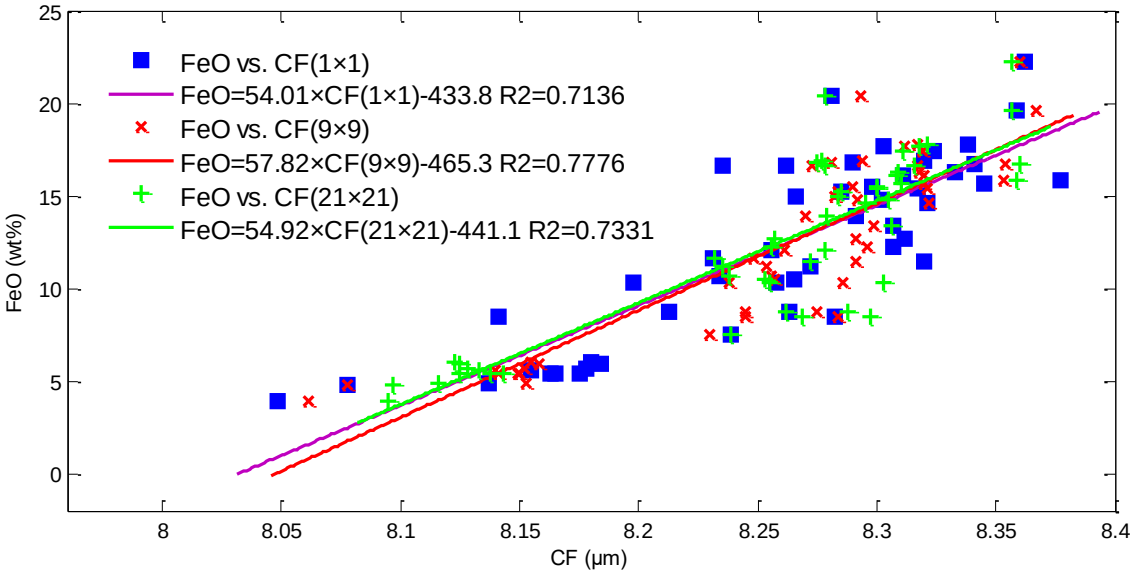

418

419 Figure 7. The relationships between FeO abundances and Diviner CF for 1×1 (blue square), 9×9 (red cross), 21×21
420 (green cross) pixels at 48 sampling sites. The regression slopes (a, b) and R^2 are shown in legend. The R^2 for 1×1, 3×3,
421 5×5, 7×7, 9×9, 11×11, 13×13, 15×15, 17×17, 19×19, 21×21 pixels are 0.7136, 0.7395, 0.7713, 0.7716, 0.7776, 0.7636,
422 0.7570, 0.7534, 0.7476, 0.7399, 0.7331 respectively. The maximum R^2 is 0.7776 with 9×9 pixels.

423 The other is the RMSE limitations of 48 datasets. In Table 5, the initial R^2 show that SiO_2, TiO_2,
424 MgO and CaO abundances are not closely correlated with Diviner CF. Under the limitations of 1.5
425 and 1 initial RMSE, dozens of outliers are eliminated. The correlations are not radically changed. But,
426 the coefficients (p1, p2 or a, b) are slightly adjusted and the R^2 increase significantly especially for
427 SiO_2 from 0.1546 to 0.604.

428 Table 5 The relationships between elemental abundances and Diviner CF under the limitations of 1, 1.5, initial RMSE

Coefficients	Initial RMSE					
	SiO_2(48)	TiO_2(48)	Al_2O_3(48)	FeO(48)	MgO(48)	CaO(48)
p1 or a	-11.28	4.053e-64	-64.77	54.01	16.33	-20.36
p2 or b	137.4	69.61	552.7	-433.8	-125.7	180.3
R^2	0.1546	0.3894	0.7491	0.7136	0.4655	0.5376
RMSE	1.991	2.241	2.858	2.608	1.334	0.5276
Coefficients	1.5 * initial RMSE					
	SiO_2(42)	TiO_2(43)	Al_2O_3(42)	FeO(42)	MgO(43)	CaO(43)
p1 or a	-8.19	1.692e-77	-65.15	53.31	20.74	-21.41
p2 or b	112.2	84.11	556.1	-428.3	-162.1	189.1
R^2	0.1341	0.5935	0.8224	0.8248	0.6868	0..6923
RMSE	1.619	1.410	2.408	1.944	1.043	1.097
Coefficients	1.0 * initial RMSE					
	SiO_2(30)	TiO_2(38)	Al_2O_3(31)	FeO(35)	MgO(31)	CaO(33)
p1 or a	-13.06	7.473e-75	-63.46	57.56	19.25	-19.47
p2 or b	151.5	81.24	541.8	-463.3	-149.9	172.9
R^2	0.604	0.704	0.9043	0.8843	0.7853	0.7504
RMSE	0.8859	1.106	1.67	1.563	0.7589	0.833

Meanwhile, from the perspective of remote sensing theory, spectral values or sampling elemental abundances can better describe the mixed pixel information with highest resolution. Therefore, the latter method is adopted in our study. Under 1 initial RMSE, the elemental abundances and Diviner CF of 1×1 pixel at 48 sampling sites are the data sources for Diviner models.

4.2 Comparison with previous work

The similar results with six Diviner elemental abundances had been investigated by Clementine UV-VIS data (Lucey et al., 2000), LP GR data (Prettyman et al., 2006) and CE-1 IIM data (Wu, 2012; Xia et al., 2019). They can also be compared to each other. Because of the different resolution, the comparisons are performed from the 47 verification points, lunar geological units and three separate surfaces.

4.2.1 Point elemental abundances

The average abundances from 47 verification points are extracted including 33 points from 150°W to 150°E and 30°N to 30°S, 2 CE sampling points, 3 pyroclastic deposit points (Allen et al., 2012), northwestern farside highland (NWFH), southern nearside highland (SNH) and northeastern farside highland (NEFH) points (Wu, 2012), 2 SPA points, Plato point and 3 mare points (Figure 6, red points). The verification area size is 0.078125°×0.078125° where latitude and longitude in the lower left corner are the reference. In this way, the number of extracted pixels of LP, Clementine, Diviner and CE-1 are 1, 4, 64 and 90-100 respectively before deleting the null values.

Table 6 shows the Pearson Correlation Coefficients (PCC) of 47 average elemental abundances for six results. The PCC between Diviner and LP are lower than that between Diviner and other results. There are the highest correlations between Diviner and CE-1 (Wu) for SiO_2 and MgO (0.8861 of PCC). For the other four oxides, the highest correlations are between Diviner and CE-1 (Xia) that the highest PCC of TiO_2 is 0.0.9414 and the lowest PCC of CaO is 0.9176.

Table 6 the PCC of 47 average elemental abundances for five results each other.

data	Diviner						LP					
	SiO2	TiO2	Al2O3	FeO	MgO	CaO	SiO2	TiO2	Al2O3	FeO	MgO	CaO
LP	-	0.4675	0.7296	0.8263	0.6668	0.5734	-	1	1	1	1	1
Clementine	-	0.7343	-	0.8846	-	-	-	0.4239		0.9229	-	-
CE-1(wu)	0.8861	0.8379	0.8862	0.9067	0.8861	0.8862	-	0.2036	0.6880	0.8755	0.6145	0.6634
CE-1(Xia)	0.6813	0.9414	0.9363	0.9397	0.7210	0.9176	-	0.5668	0.8916	0.9014	0.6496	0.8904
Diviner	1	1	1	1	1	1	-	0.4675	0.7296	0.8263	0.6668	0.5734

data	CE-1 (Wu)						CE-1 (Xia)					
	SiO2	TiO2	Al2O3	FeO	MgO	CaO	SiO2	TiO2	Al2O3	FeO	MgO	CaO
LP	-	0.2036	0.6880	0.8755	0.6145	0.6634	-	0.5668	0.8916	0.9014	0.6496	0.8904
Clementine	-	0.7227	-	0.9118	-	-	-	0.8137	-	0.9542	-	-
CE-1(Wu)	1	1	1	1	1	1	0.6480	0.8827	0.9220	0.9510	0.7664	0.9015
CE-1(Xia)	0.6480	0.8827	0.9220	0.9510	0.7664	0.9015	1	1	1	1	1	1
Diviner	0.8861	0.8379	0.8862	0.9067	0.8861	0.8862	0.8861	0.9414	0.9363	0.9397	0.7210	0.9176

Description: The resolution of LP SiO2 is 20°×20°. The SiO2, Al2O3, MgO and CaO results by Clementine are not achieved. The comparisons with these results are not made.

Diviner results match well with Clementine and CE-1 results and bad with LP results. Except for the detecting methods and depths in different techniques, the reason is the lower resolution of LP results. With the resolution of 0.5°×0.5° for TiO_2 and FeO or 5°×5° for Al_2O_3, MgO and CaO, only one LP pixel value which represents the elemental abundance for 0.5°×0.5° or 5°×5° can be extracted. Hence, LP elemental abundances of verification points are inaccurate. As the resolution increasing, the difference is getting smaller and smaller in the verification points between Diviner and Clementine or CE-1 results.

Meanwhile, the maximum deviations of SiO_2 and MgO between Diviner and CE-1 (Wu) are 1.7569 wt.% at SPA2 (165°E, 45°S) and 3.0087 wt.% at 0°, 30°S respectively. The maximum deviations of TiO_2, Al_2O_3 FeO and CaO between Diviner and CE-1 (Xia) are 2.0804 wt.% at Sulpicius Gallus (10.283°E, 20.15°N), 4.2496 wt.% at SPA2 (165°E, 45°S), 2.8902 wt.% at 60°E, 0°, and 1.2622 wt.% at SPA2 (165°E, 45°S) respectively. It is obvious that the deviations of average elemental abundances on highland or SPA basin surface are higher than that on mare surfaces. The reason is that the data sources used in the establishment of the models mainly come from mare data except for Apollo 17. In this way, there are many uncertainties on the highland or SPA basin surface which would led to the variations in different results.

4.2.2 Regional elemental abundances

The differences of elemental abundances on global or lunar geological unit's surfaces also have comparative significance. The average elemental abundances are extracted from the global, maria, highland, SPA basin surfaces after deleting the null values and outliers (Figure 8).

On the global surfaces (Figure 8, a), Diviner SiO_2, FeO and MgO abundances are consistent with CE-1 (Wu) results and the differences are 0.02, 0.09 and 0.42 wt.%. Diviner TiO_2 abundance are consistent with Clementine results and the difference is 0.15 wt.%. Diviner Al_2O_3 and CaO abundances are consistent with CE-1 (Xia) and the differences are 0.1 and 0.37 wt.%. With the exception of SiO_2 and FeO, other four Diviner elemental abundances are quite different from LP results and the maximum difference is 10.84 wt.% of Al_2O_3.

On the mare surfaces (Figure 8, b), Diviner TiO_2 abundance is lowest and MgO abundance is highest in all results. The consistency correlation between Diviner results and other four results has hardly changed. But, the differences are increasing compared to global surfaces except for MgO and CaO. On the highland (Figure 8, c) and SPA basin (Figure 8, d) surfaces, Diviner FeO abundance is lowest and Al_2O_3 abundance is highest in all results. The elemental abundances of six datasets are disorderly and unsystematic. The difference between any two datasets is almost decreasing on highland surface and increasing on SPA surface.

There are two main reasons for this consistency results. One may be related to the resolution of the data. Under the premise, the data missing and derivation error problems are ignored. With the improvement of resolution, more and more pixels of higher or lower elemental abundances are identified which leads to the closer average between Diviner and Clementine or CE-1 especially on a global scale. The other is the area of the comparison region. On larger surfaces such as global or highland, the difference information is integrated and reduced which is the opposite on smaller

surfaces such as maria or SPA.

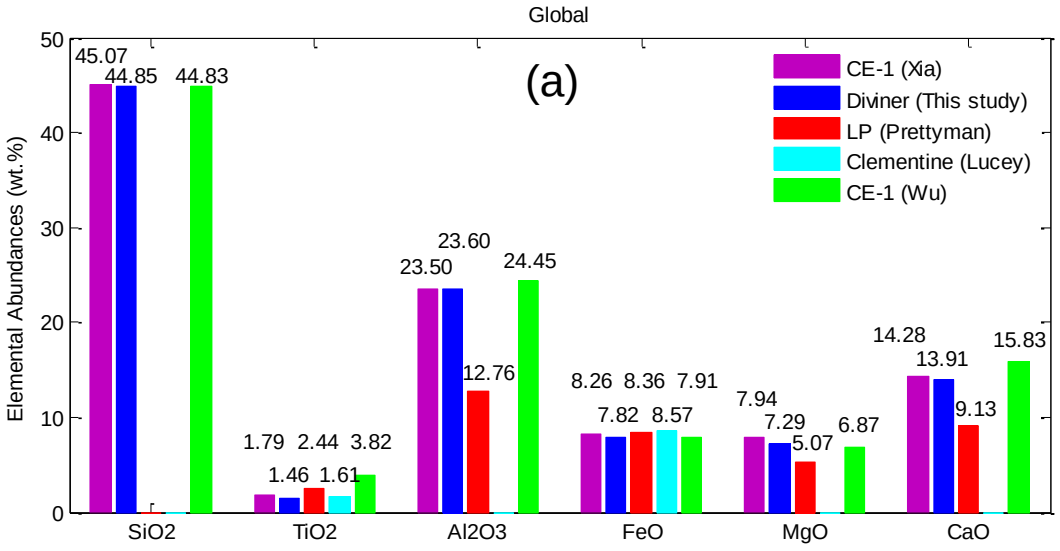

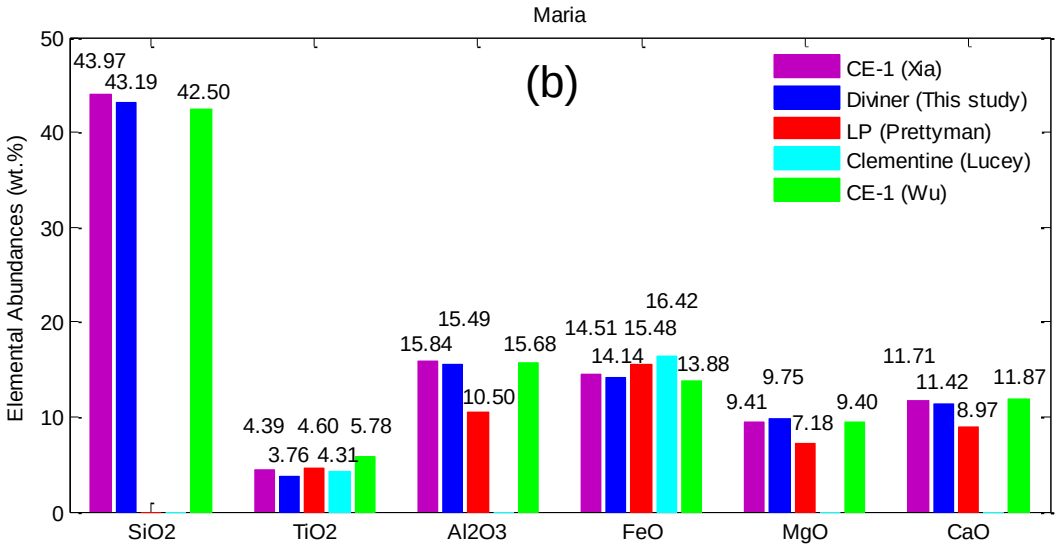

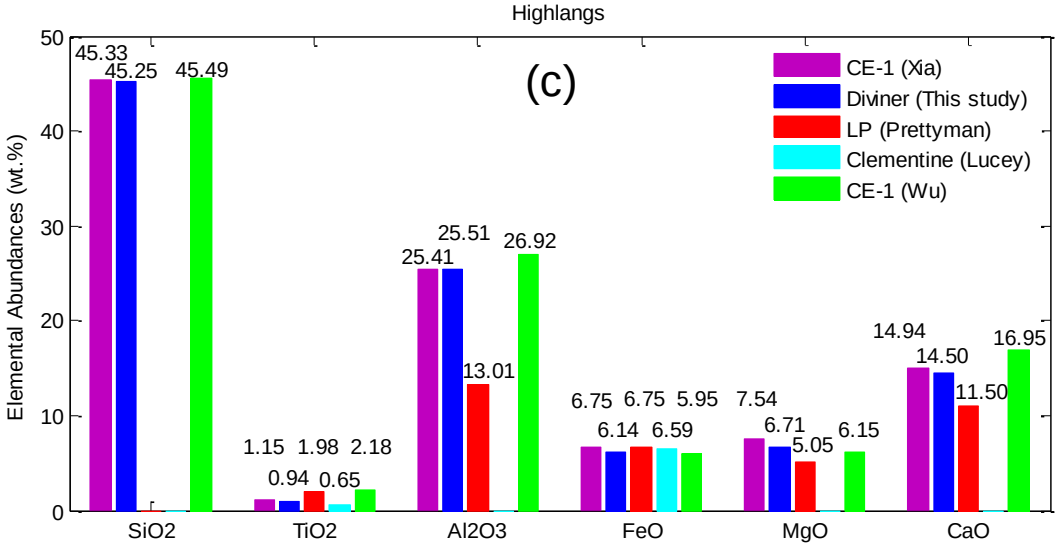

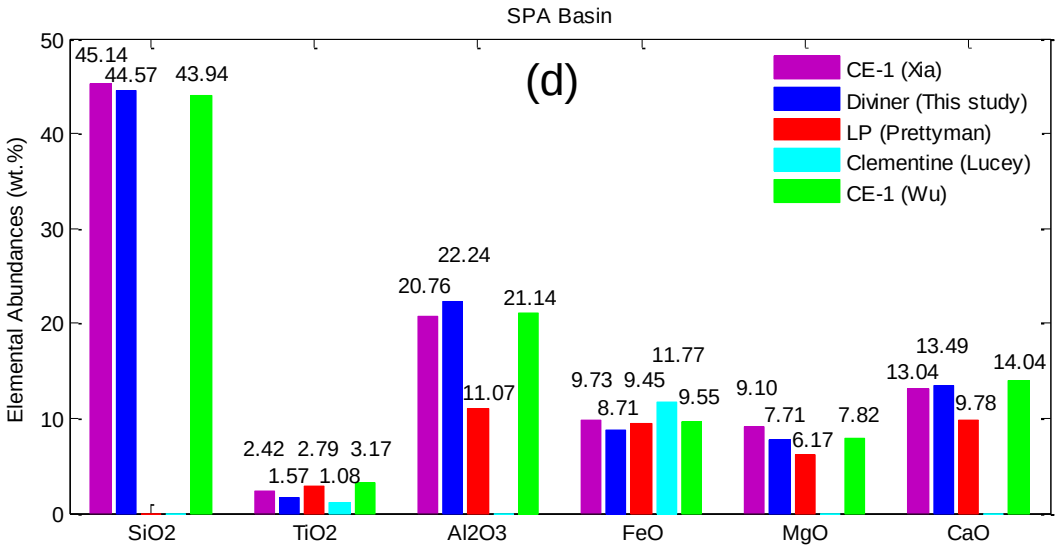

Figure 8. The average elemental abundances after deleting the null values extracted from the global (a), maria (b), highland (c), SPA (d) surface derived by Diviner, LP, Clementine, CE-1.

4.2.3 The elemental abundances on three separate surfaces

The comparisons from points and regions indicate that Diviner results are consistent with Clementine and CE-1 results. However, the advantages of Diviner results have not been shown especially on the surfaces with high latitudes or poor light conditions. In this study, three separate surfaces with different latitudes and geological types - Plato crater, Mare Humboldtianum, and the highlands between Mare Insularum and Mare Imbrium have been investigated.

Figure 9 shows the FeO images of five results on Plato crater and surrounding highland surfaces (4°-15°W, 49°-54°N). Diviner FeO (Figure 9, a) show a similar distribution with CE-1 FeO of Xia et al. (2019) (Figure 9, b), but the coverage is obviously higher. Except for the null values in CE-1 IIM, there are a lot of zeros in the FeO image of Wu (2012) (Figure 9, c) because of the shadow. There are many discrepancies for Clementine FeO of Lucey et al. (2000) (Figure 9, d) around the rim of Plato crater particularly in the northwest and southeast. The usefulness of LP FeO of Prettyman et al. (2006) (Figure 9, e) is clearly limited to a small area.

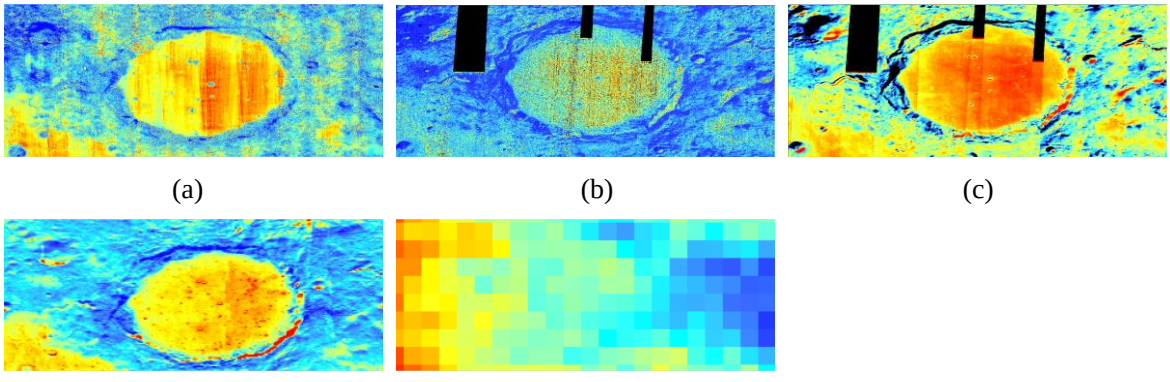

(a) (b) (c)

(d) (e)

Figure 9. The FeO images of Diviner (a), CE-1 (Xia et al., 2019) (b), CE-1 (Wu, 2012) (c), Clementine (Lucey et al., 2000) (c) and LP (Prettyman et al., 2006) (e) results on Plato crater surface (4°-15°W, 49°-54°N). Black pixels are null values or 0. The image scale is 1:4,000,000.

For TiO_2 on Mare Humboldtianum surface (74.7°-86.7°E, 54.1°-58.8°N) at high latitudes (figure 10), the above problems are more obvious. The low coverage seriously affects the availability of CE-1 IIM (figure 10, b and c). The discrepancies for Clementine TiO_2 of Lucey et al. (2000) (Figure 10, d) are bigger.

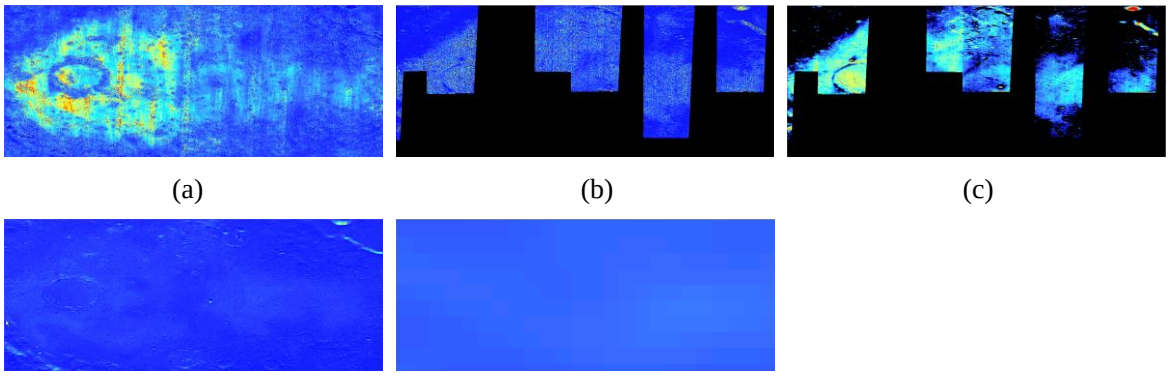

(a) (b) (c)

(d) (e)

Figure 10. The TiO_2 images of Diviner (a), CE-1 (Xia et al., 2019) (b), CE-1 (Wu, 2012) (c), Clementine (Lucey et al., 2000) (c) and LP (Prettyman et al., 2006) (e) results on Mare Humboldtianum surface (74.7°-86.7°E, 54.1°-58.8°N). Black pixels are null values or 0. The image scale is 1:4,500,000.

For Al_2O_3 on highland surface (12.2°-33.6°W, 6.4°-14.8°N) at low latitudes (figure 11), the consistency between Diviner Al_2O_3 and CE-1 Al_2O_3 is satisfactory with the disappearing of the shadow. But, the coverage of CE-1 IIM and The usefulness of LP gamma ray data have not improved significantly

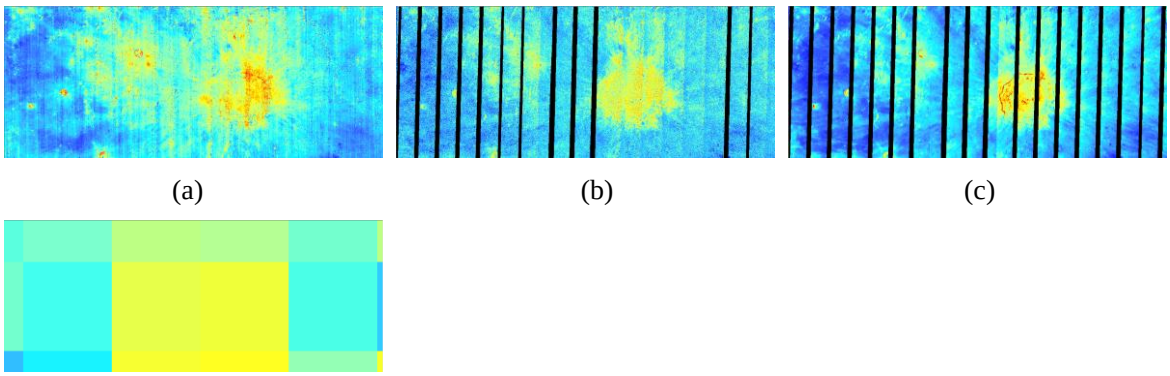

(a) (b) (c)

(d)

Figure 11. The Al_2O_3 images of Diviner (a), CE-1 (Xia et al., 2019) (b), CE-1 (Wu, 2012) (c), and LP (Prettyman et al., 2006) (d) results on highland surface (74.7°-86.7°E, 54.1°-58.8°N) between Mare Insularum and Mare Imbrium. Black pixels are null values or 0. The image scale is 1:8,000,000.

Therefore, Diviner elemental abundance maps are the best results until now not only considering both resolution and coverage simultaneously, but also on the surfaces with high latitudes or poor light conditions. Furthermore, with the calculation of CF in Polar Regions, the usefulness of Diviner results will be greater.

4.3Geological applications

4.3.1 Classification of mare basalts

The lunar basalts cover >17% lunar surface and constitute <1% lunar crust volume. They record information on composition, mineralogy and geological evolution process from depths of 200-400 kilometers. Based on TiO_2 and Al_2O_3 abundances of lunar samples, Neal and Taylor (1992) had classified the mare basalt into six rock types. The TiO_2 classifications were very low-Ti (<1wt.% TiO_2), low-Ti (1-6 wt.% TiO_2) and high-Ti (6-14 wt.% TiO_2). The Al_2O_3 classifications were low-Al (<11 wt.% Al_2O_3) and high-Al (>11 wt.% Al_2O_3). With TiO_2 and Al_2O_3 abundance maps of Figure 5 (b, c), the classifications are applied. In Figure 12, the results indicate that (1) low-Ti mare basalts widely distributed on mare surfaces. (2) high-Ti and low-Al mare basalts are mainly concentrated in Mare Tranquillitatis and scattered in Mare Imbrium (middle), Oceanus Procellarum (south), Mare Fecunditatis (north) and Mare Serenitatis (around). (3) very low-Ti mare basalts are mainly concentrated in several impact craters or volcanic craters in Oceanus Procellarum and Mare Frigoris, and distributed in the boundary region between maria and highland. (4) high-Al mare basalts are mainly concentrated in Mare Frigoris, Mare Nubium, Mare Australe and the mare surfaces surrounded by highland such as Mare Orientale and Mare Humboldtianum.

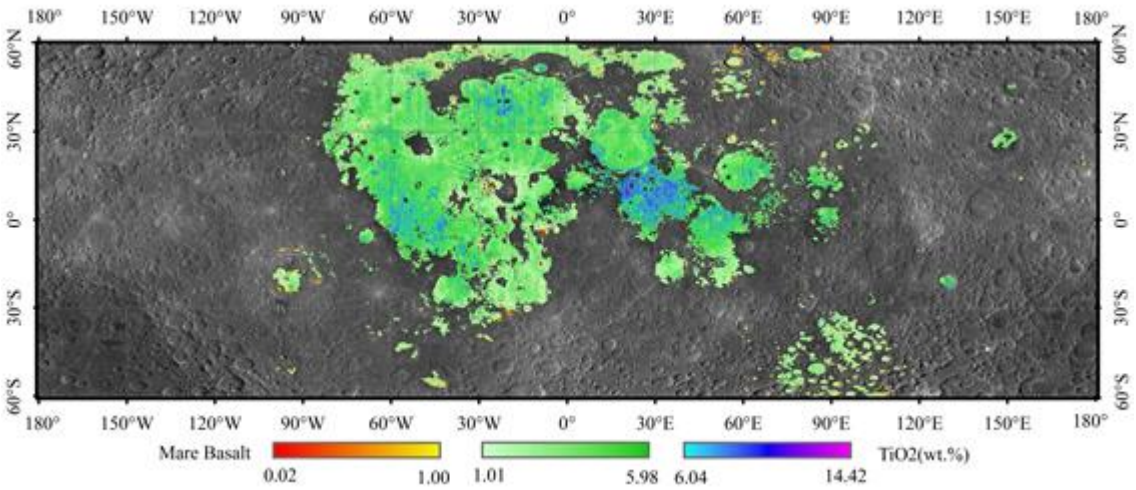

(a)

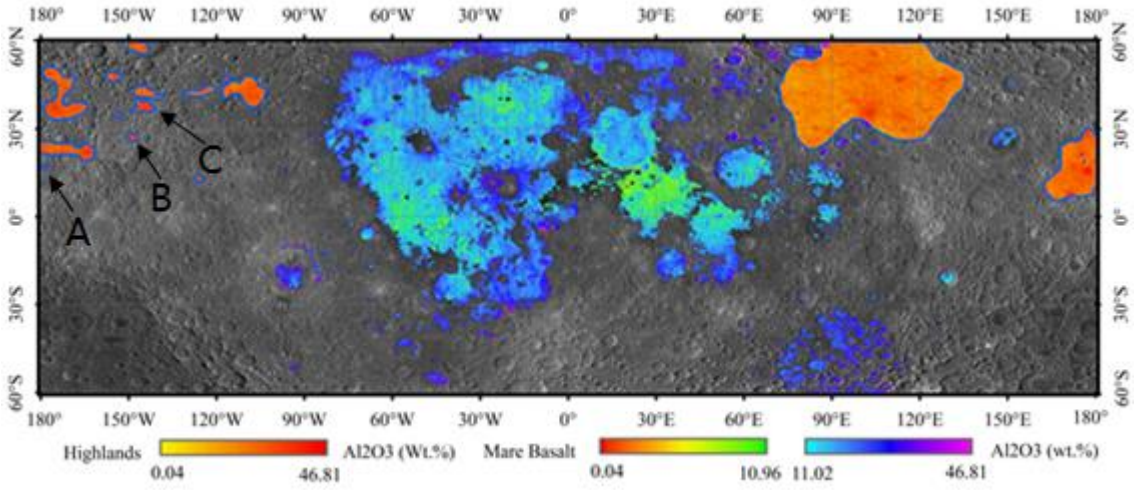

(b)

Figure 12. The classification map of mare basalts based on TiO_2 (a) and Al_2O_3 (b) abundances. Referring to Figure 2 for geographic information and base map. The blue polylines in Al_2O_3 mare basalts map (b) are 15 highland surface with higher Al_2O_3 abundances.

4.3.2 Inhomogeneity of highland crust

In lunar magma ocean hypothesis, the fractionation and crystallization events of plagioclase imply that the lunar crust is uniform. However, lunar crustal heterogeneity had been discussed from the perspective of chemistry (Jolliff et al., 2000) and mineralogy (Pieters, 1993). Jolliff et al. (2000) concluded that the thickest part of lunar crust had highest Al_2O_3, abundance (29 wt.%) and lowest FeO abundance (4.2 wt.%) and was centered around 40°N, 180°E. According to this standard, 15 highland surface are found on the farside (Figure 12, b, blue polylines) and the average Al_2O_3 and FeO abundances are displayed in Table 7. Only considering chemical elemental abundances, the lunar crust is probably the thickest on three highland surfaces with the central position of 178°W17°N (Figure 12, A), 148°W28°N (Figure 12, B) and 145°W38°N (Figure 12, C) which have the highest Al_2O_3 and lowest FeO abundances. Meanwhile, the order of SiO_2, Al_2O_3, CaO is northwestern> northeastern> southern on highland surfaces, while the order of CF, TiO_2, FeO, MgO is opposite. It indicates that the highland crust is inhomogenous not only between northern and southern (Wu, 2012), but also between northwestern and northeastern.

Table 7 The average Al_2O_3 and FeO abundances (wt.%) of 15 highland surface

Central Position	175°W 37°N	164°W 22°N	178°W 17°N	146°W 59°N	155°W 48°N	153°W 35°N	148°W 28°N	145°W 43°N
Al_2O_3	30.13	31.24	**31.41**	29.24	28.49	30.32	**32.78**	31.27
FeO	3.52	2.17	1.74	4.80	4.39	3.43	2.14	3.79

Central Position	145°W 38°N	126°W 14°N	125°W 43°N	116°W 47°N	110°W 44°N	99°E 45°N	173°E 17°N
Al_2O_3	**33.53**	29.36	29.96	27.98	29.58	26.48	28.87
FeO	2.87	2.59	3.87	5.08	3.46	5.52	3.10

4.3.3 Diviner Mg#

Mg# is one of the most important parameters in lunar petrology which can characterize the composition changes during the cooling and crystallizing of lunar magma. With the FeO and MgO abundances maps of Figure 5 (d, e), the molar ratio of Mg/(Mg+Fe) can be calculated (Figure 13). The global mean of Mg# is 48.49. Comparing with Clementine, LP and CE-1 Mg# (Lucey, 2004; Prettyman et al., 2006; Wu, 2012; Crites and Lucey, 2015; Xia et al., 2019), Diviner Mg# are significantly lower. The reason may be due to the detecting methods and depths. However, Diviner Mg# can better show the sequence and results of cooling and crystallizing of lunar magma. For example, the differences of Diviner Mg# between mare and highland surface are bigger that the maximum Mg# is 99.99 and the minimum Mg# is 28.21. The inhomogenous distribution of Diviner Mg# on highland surface is more obvious but it is nearly uniform on mare surfaces. The highland Mg# of > 30°N are higher than that of other highland surface except for the SPA surface. Meanwhile, a preliminary trial that the boundaries of three lunar crustal terranes are determined by Diviner Mg#

is carried out (Figure 13, red polyline) including the Procellarum KREEP Terrane (PKT), The Feldspathic Highland Terrane (FHT) and the South Pole-Aitken Terrane (SPAT) identified by Jolliff et al. (2000).

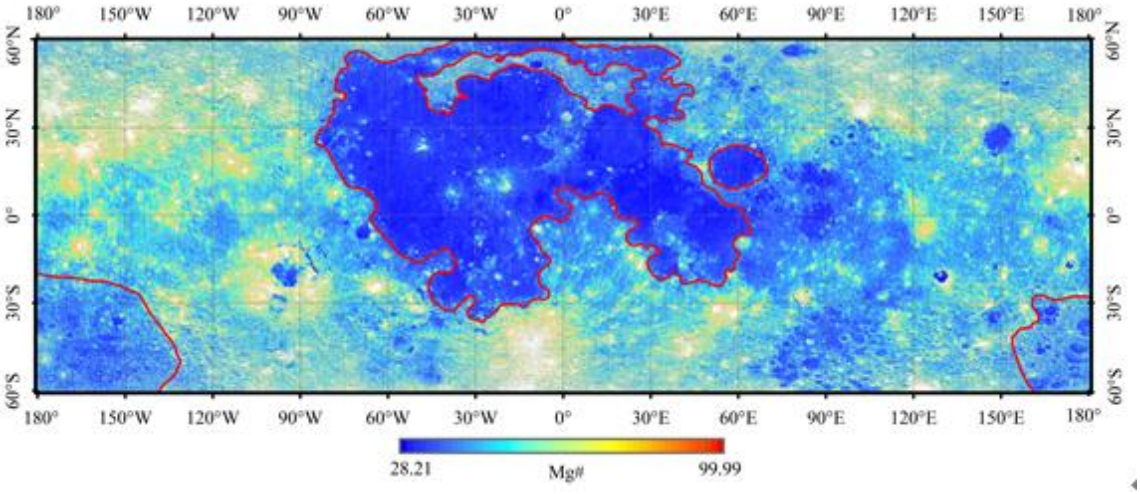

Figure 13. The Mg# map and the boundaries of three lunar crustal terranes (red polyline). Referring to Figure 2 for geographic information.

5. Conclusions

The Diviner models are the "global" thermal infrared models from all available lunar sampling sites and make it feasible to estimate the elemental abundances on lunar surface. Although the models are relatively simple and require 1 RMSE of 48 datasets as the limitations, Diviner CF are clearer correlated with elemental abundances than diagnostic characteristics of electron transition. The overall global results agree well with the models. The highest R^2 is 0.9043 for Al_2O_3 and the lowest R^2 is 0.604 for SiO_2.

The Diviner CF images with high both resolution and coverage can assist in acquiring detailed information about the elemental abundances and distribution on a global scale. Therefore, the new six oxide abundance images between 60°N/S based on Diviner Level 3 Standard CF product are presented in this study. The global average elemental abundances of SiO_2, TiO_2, Al_2O_3, FeO, MgO and CaO are 44.85 wt.%, 1.46 wt.%, 23.60 wt.%, 7.82 wt.%, 7.29 wt.% and 13.91 wt.% respectively.

Comparing with Clementine (Lucey et al., 2000), LP (Prettyman et al., 2006) and CE-1 (Wu, 2012; Xia et al., 2019) results from points, regions and three separate surfaces, Diviner results are consistent with Clementine and CE-1 results and less with LP results. In addition, considering both resolution and coverage simultaneously, Diviner elemental abundance images are the best results until now. These not only provide more detailed elemental abundance information than UV-VIS, GR, IIM images on a global scale or local surfaces, but also have higher accuracy especially on the surface with high latitudes or poor light conditions. Meanwhile, Diviner elemental abundance images are also effective and reliable for solving the lunar geological problems including classifications of mare basalt, inhomogeneity of highland crust and Mg#.

There are certain limitations for the study. Diviner elemental abundance images only cover

two-thirds of the moon and the CF of Polar Regions has not been carried out. In future, the calculation of Diviner CF image and elemental abundances with the resolution of 128 pixels/degree will be planned in Polar Regions where the elemental abundances of Clementine and Chang'E-1 have not been implemented.

Acknowledgments

We thank the reviewers and editors for their hard work and valuable suggestions. We thank the LRO Diviner operations teams and The PDS Geosciences Node Lunar Orbital Data Explorer (ODE) at Washington University in St. Louis for their support in ten years. We thank Dr. Yunzhao Wu and Dr. Wang Xianmin for providing elemental abundance and Mg# maps based on CE-1 IIM data and especially for their constructive suggestions on this paper. This research was jointly Supported by National Natural Science Foundation of China (41372337, 3A415AK44423, 41772346), Special project of science and Techniques Foundation (2015FY210500), the National High Techniques Research and Development Program ("863" Program) of China (2015AA123704).

The Diviner SiO_2, TiO_2, Al_2O_3, FeO, MgO and CaO abundance and Mg# images are available in Harvard Dataverse and the DOI is https://doi.org/10.7910/DVN/ADSUJD. All Diviner RDR and GDR data come from http://ode.rsl.wustl.edu/moon/indexProductSearch.aspx. The Clementine UVVIS data and Lunar Prospector Gamma Ray Spectrometer Elemental Abundance are available at https://planetarymaps.usgs.gov/mosaic/ and ftp://pds-geosciences.wustl.edu/lunar/lp-l-grs-5-elem-abundance-v1/.

References

Adler, I., Trombka, J., Gerard, J., Lowman, P., Schmadebeck, R., Blodget, H., & Bjorkholm, P. (1972). Apollo 15 geochemical X-ray fluorescence experiment: Preliminary report. *Science*, *175*(4020), 436-440.

Adler, I., Trombka, J. T., Lowman, P., Schmadebeck, R., Blodget, H., Eller, E., & Gursky, H. (1973). Results of the Apollo 15 and 16 x-ray fluorescence experiment. *Lunar Science IV, edited by JW Chamberlain and C. Watkins*, 9.

Allen, C. C., Greenhagen, B. T., Donaldson Hanna, K. L., & Paige, D. A. (2012). Analysis of lunar pyroclastic deposit FeO abundances by LRO Diviner. *Journal of Geophysical Research: Planets*, *117*(E12).

Athiray, P. S., Narendranath, S., Sreekumar, P., Dash, S. K., & Babu, B. R. S. (2013). Validation of methodology to derive elemental abundances from X-ray observations on Chandrayaan-1. *Planetary and Space Science*, *75*, 188-194.

Blewett, D. T., Lucey, P. G., Hawke, B. R., & Jolliff, B. L. (1997). Clementine images of the lunar sample‐return stations: Refinement of FeO and TiO2 mapping techniques. *Journal of Geophysical Research: Planets*, *102*(E7), 16319-16325.

Burns, R. G. (1970). Crystal field spectra and evidence of cation ordering in olivine minerals. *American Mineralogist: Journal of Earth and Planetary Materials*, *55*(9-10), 1608-1632.

Charette, M. P., McCord, T. B., Pieters, C., & Adams, J. B. (1974). Application of remote spectral reflectance measurements to lunar geology classification and determination of titanium content of lunar soils. *Journal of Geophysical Research*, *79*(11), 1605-1613.

671 Charette, M. P., Taylor, S. R., Adams, J. B., & McCord, T. B. (1977). The detection of soils of Fra
672 Mauro basalt and anorthositic gabbro composition in the lunar highlands by remote spectral
673 reflectance techniques. In *Lunar and Planetary Science Conference Proceedings* (Vol. 8, pp.
674 1049-1061).
675 Crites, S. T., & Lucey, P. G. (2015). Revised mineral and Mg# maps of the Moon from integrating
676 results from the Lunar Prospector neutron and gamma-ray spectrometers with Clementine
677 spectroscopy. *American Mineralogist*, *100*(4), 973-982.
678 Conel, J. E. (1969). Infrared emissivities of silicates: Experimental results and a cloudy
679 atmosphere model of spectral emission from condensed particulate mediums. *Journal of*
680 *Geophysical Research*, *74*(6), 1614-1634.
681 Donaldson Hanna, K. L., Wyatt, M. B., Thomas, I. R., Bowles, N. E., Greenhagen, B. T., Maturilli,
682 A., & Paige, D. A. (2012). Thermal infrared emissivity measurements under a simulated lunar
683 environment: Application to the Diviner Lunar Radiometer Experiment. *Journal of*
684 *Geophysical Research: Planets*, *117*(E12).
685 Dong, W. D., Zhang, X. P., Zhu, M. H., Xu, A. A., & Tang, Z. S. (2016). Global Mg/Si and Al/Si
686 Distribution on the Lunar Surface Derived from Chang'E-2 X-ray Spectrometer. *Research in*
687 *Astronomy and Astrophysics*, *16*(1), 004.
688 Elphic, R. C., Lawrence, D. J., Feldman, W. C., Barraclough, B. L., Maurice, S., Binder, A. B., &
689 Lucey, P. G. (1998). Lunar Fe and Ti abundances: comparison of Lunar Prospector and
690 Clementine data. *Science*, *281*(5382), 1493-1496.
691 Elphic, R. C., Lawrence, D. J., Feldman, W. C., Barraclough, B. L., Maurice, S., Binder, A. B., &
692 Lucey, P. G. (2000). Lunar rare earth element distribution and ramifications for FeO and TiO2:
693 Lunar Prospector neutron spectrometer observations. *Journal of Geophysical Research:*
694 *Planets*, *105*(E8), 20333-20345.
695 Elphic, R. C., Lawrence, D. J., Feldman, W. C., Barraclough, B. L., Gasnault, O. M., Maurice,
696 S., ... & Binder, A. B. (2002). Lunar Prospector neutron spectrometer constraints on
697 TiO2. *Journal of Geophysical Research: Planets*, *107*(E4), 8-1.
698 Feldman, W. C., Barraclough, B. L., Maurice, S., Elphic, R. C., Lawrence, D. J., Thomsen, D. R.,
699 & Binder, A. B. (1998). Major compositional units of the Moon: Lunar Prospector thermal and
700 fast neutrons. *Science*, *281*(5382), 1489-1493.
701 Feldman, W. C., Lawrence, D. J., Elphic, R. C., Vaniman, D. T., Thomsen, D. R., Barraclough, B.
702 L., & Binder, A. B. (2000). Chemical information content of lunar thermal and epithermal
703 neutrons. *Journal of Geophysical Research: Planets*, *105*(E8), 20347-20363.
704 Fischer, E. M., & Pieters, C. M. (1994). Remote determination of exposure degree and iron
705 concentration of lunar soils using VIS-NIR spectroscopic methods. *Icarus*, *111*(2), 475-488.
706 Fischer, E. M., & Pieters, C. M. (1996). Composition and exposure age of the Apollo 16 Cayley
707 and Descartes regions from Clementine data: Normalizing the optical effects of space
708 weathering. *Journal of Geophysical Research: Planets*, *101*(E1), 2225-2234.
709 Grande, M., Dunkin, S., Howe, C., Browning, R., Kellett, B., Perry, C. H., & Thomas, N. (2004).
710 Lunar elemental composition and ivestigations with D-CIXS x-ray mapping spectrometer on
711 SMART-1.
712 Greenhagen, B. T., Lucey, P. G., Wyatt, M. B., Glotch, T. D., Allen, C. C., Arnold, J. A., ... & Song,
713 E. (2010). Global silicate mineralogy of the Moon from the Diviner Lunar
714 Radiometer. *Science*, *329*(5998), 1507-1509.

Hapke, B. W., Cohen, A. J., Cassidy, W. A., & Wells, E. N. (1970). Solar radiation effects on the optical properties of Apollo 11 samples. *Geochimica et Cosmochimica Acta Supplement*, *1*, 2199.

Heiken, G. H., Vaniman, D. T., & French, B. M. (1991). Lunar sourcebook-A user's guide to the moon. *Research supported by NASA,. Cambridge, England, Cambridge University Press, 1991, 753 p.*.

Jolliff, B. L. (1999). Clementine UVVIS multispectral data and the Apollo 17 landing site: What can we tell and how well?. *Journal of Geophysical Research: Planets*, *104*(E6), 14123-14148.

Jolliff, B. L., Gillis, J. J., Haskin, L. A., Korotev, R. L., & Wieczorek, M. A. (2000). Major lunar crustal terranes: Surface expressions and crust‐mantle origins. *Journal of Geophysical Research: Planets*, *105*(E2), 4197-4216.

Lawrence, D. J., Feldman, W. C., Barraclough, B. L., Binder, A. B., Elphic, R. C., Maurice, S., & Thomsen, D. R. (1998). Global elemental maps of the Moon: The Lunar Prospector gamma-ray spectrometer. *Science*, *281*(5382), 1484-1489.

Lawrence, D. J., Feldman, W. C., Barraclough, B. L., Binder, A. B., Elphic, R. C., Maurice, S., & Prettyman, T. H. (1999). High resolution measurements of absolute thorium abundances on the lunar surface. *Geophysical Research Letters*, *26*(17), 2681-2684.

Lawrence, D. J., Feldman, W. C., Barraclough, B. L., Binder, A. B., Elphic, R. C., Maurice, S., ... & Prettyman, T. H. (2000). Thorium abundances on the lunar surface. *Journal of Geophysical Research: Planets*, *105*(E8), 20307-20331.

Lawrence, D. J., Feldman, W. C., Elphic, R. C., Little, R. C., Prettyman, T. H., Maurice, S., ... & Binder, A. B. (2002). Iron abundances on the lunar surface as measured by the Lunar Prospector gamma‐ray and neutron spectrometers. *Journal of Geophysical Research: Planets*, *107*(E12), 13-1.

Ling, Z., Zhang, J., Liu, J., Zhang, W., Bian, W., Ren, X., ... & Li, C. (2011). Preliminary results of FeO mapping using Imaging Interferometer data from Chang'E-1. *Chinese Science Bulletin*, *56*(4-5), 376-379.

Liu, B., DI, K., Wang, B., Tang, G., Xu, B., Zhang, L., & Liu, Z. (2015). Positioning and precision validation of Chang'E -3 Lander based on multiple LRO NAC images. *Chinese Science Bulletin, 60*(28-29), 2750-2757.

Lucey, P. G., Taylor, G. J., & Malaret, E. (1995). Abundance and distribution of iron on the Moon. *Science*, *268*(5214), 1150-1153.

Lucey, P. G., Blewett, D. T., & Hawke, B. R. (1998). Mapping the FeO and TiO2 content of the lunar surface with multispectral imagery. *Journal of Geophysical Research: Planets*, *103*(E2), 3679-3699.

Lucey, P. G., Blewett, D. T., & Jolliff, B. L. (2000). Lunar iron and titanium abundance algorithms based on final processing of Clementine ultraviolet‐visible images. *Journal of Geophysical Research: Planets*, *105*(E8), 20297-20305.

Lucey, P., Korotev, R. L., Gillis, J. J., Taylor, L. A., Lawrence, D., Campbell, B. A., & Mendillo, M. (2006). Understanding the lunar surface and space-Moon interactions. *Reviews in Mineralogy and Geochemistry*, *60*(1), 83-219.

McCord, T. B., & Adams, J. B. (1973). Progress in remote optical analysis of lunar surface composition. *Moon*, *7*, 453-474.

McCord, T. B., & Adams, J. B. (1973). Progress in remote optical analysis of lunar surface composition. *Moon, 7*, 453-474.

McCord, T. B., Clark, R. N., Hawke, B. R., McFadden, L. A., Owensby, P. D., Pieters, C. M., & Adams, J. B. (1981). Moon: Near‐infrared spectral reflectance, a first good look. *Journal of Geophysical Research: Solid Earth*, *86*(B11), 10883-10892.

Metzger, A. E., Trombka, J. I., Reedy, R. C., & Arnold, J. R. (1974). Element concentrations from lunar orbital gamma-ray measurements. In *Lunar and Planetary Science Conference Proceedings* (Vol. 5, pp. 1067-1078).

Metzger, A. E., Haines, E. L., Parker, R. E., & Radocinski, R. G. (1977). Thorium concentrations in the lunar surface. I-Regional values and crustal content. In *Lunar and Planetary Science Conference Proceedings* (Vol. 8, pp. 949-999).

Naito, M., Hasebe, N., Nagaoka, H., Shibamura, E., Ohtake, M., Kim, K. J., ... & Berezhnoy, A. A. (2018). Iron distribution of the Moon observed by the Kaguya gamma-ray spectrometer: Geological implications for the South Pole-Aitken basin, the Orientale basin, and the Tycho crater. *Icarus*, *310*, 21-31.

Neal, C. R., & Taylor, L. A. (1992). Petrogenesis of mare basalts: A record of lunar volcanism. *Geochimica et Cosmochimica Acta*, *56*(6), 2177-2211.

Nelson, D. M., Koeber, S. D., Daud, K., Robinson, M. S., Watters, T. R., Banks, M. E., & Williams, N. R. (2014, March). Mapping lunar maria extents and lobate scarps using LROC image products. In *Lunar and Planetary Science Conference*(Vol. 45, p. 2861).

Paige, D. A., Foote, M. C., Greenhagen, B. T., Schofield, J. T., Calcutt, S., Vasavada, A. R., & Jakosky, B. M. (2010). The lunar reconnaissance orbiter diviner lunar radiometer experiment. *Space Science Reviews*, *150*(1-4), 125-160.

Pieters, C. M. (1993). Compositional diversity and stratigraphy of the lunar crust derived from reflectance spectroscopy. *Remote Geochemical Analysis Elemental and Mineralogical Composition*, 309-339.

Pieters, C. M., & Hiroi, T. (2004, March). RELAB (Reflectance Experiment Laboratory): A NASA multiuser spectroscopy facility. In *Lunar and Planetary Science Conference* (Vol. 35).

Prettyman, T. H., Hagerty, J. J., Elphic, R. C., Feldman, W. C., Lawrence, D. J., McKinney, G. W., & Vaniman, D. T. (2006). Elemental composition of the lunar surface: Analysis of gamma ray spectroscopy data from Lunar Prospector. *Journal of Geophysical Research: Planets*, *111*(E12).

Sato, H., Robinson, M. S., Lawrence, S. J., Denevi, B. W., Hapke, B., Jolliff, B. L., & Hiesinger, H. (2017). Lunar mare TiO2 abundances estimated from UV/Vis reflectance. *Icarus*, *296*, 216-238.

Scholten, F., Oberst, J., Matz, K. D., Roatsch, T., Wählisch, M., Speyerer, E. J., & Robinson, M. S. (2012). GLD100: The near‐global lunar 100 m raster DTM from LROC WAC stereo image data. *Journal of Geophysical Research: Planets*, *117*(E12).

Sun, L., Ling, Z., Zhang, J., Li, B., Chen, J., Wu, Z., & Liu, J. (2016). Lunar iron and optical maturity mapping: Results from partial least squares modeling of Chang'E-1 IIM data. *Icarus*, *280*, 183-198.

Swinyard, B. M., Joy, K. H., Kellett, B. J., Crawford, I. A., Grande, M., Howe, C. J., ... & Wieczorek, M. A. (2009). X-ray fluorescence observations of the Moon by SMART-1/D-CIXS and the first detection of Ti Kα from the lunar surface. *Planetary and Space Science*, *57*(7), 744-750.

Tang, X., Luo, X. X., Jiang, Y., Xu, A. A., Wang, Z. C., Zhang, X. W., ... & Wu, Y. Z. (2016). Estimation of lunar FeO abundance based on imaging by LRO Diviner. *Research in Astronomy and Astrophysics*, *16*(2), 024.

Villa, A., Chanussot, J., Benediktsson, J. A., & Jutten, C. (2010). Spectral unmixing for the classification of hyperspectral images at a finer spatial resolution. *IEEE Journal of Selected Topics in Signal Processing*, *5*(3), 521-533.

Williams, J. P., Paige, D. A., Greenhagen, B. T., & Sefton-Nash, E. (2017). The global surface temperatures of the Moon as measured by the Diviner Lunar Radiometer Experiment. *Icarus*, *283*, 300-325.

Yan, B., Xiong, S. Q., Wu, Y., Wang, Z., Dong, L., Gan, F., ... & Wang, R. (2012). Mapping Lunar global chemical composition from Chang'E-1 IIM data. *Planetary and Space Science*, *67*(1), 119-129.

Wu, Y. (2012). Major elements and Mg# of the Moon: Results from Chang'E-1 interference imaging spectrometer (IIM) data. *Geochimica et Cosmochimica Acta*, *93*, 214-234.

Wu, Y., Wang, Z., Cai, W., & Lu, Y. (2018). The absolute reflectance and new calibration site of the Moon. *The Astronomical Journal*, *155*(5), 213.

Xia, W., Wang, X., Zhao, S., Jin, H., Chen, X., Yang, M., & Gao, X. (2019). New maps of lunar surface chemistry. *Icarus*, *321*, 200-215.

Wood, R. W. (1912). Selective absorption of light on the Moon's surface and lunar petrography. *The Astrophysical Journal*, *36*, 75.